Progress Towards a Primary Pressure Standard with Cold Atoms

by

Kais Jooya

B.Sc., The University of British Columbia, 2013

A THESIS SUBMITTED IN PARTIAL FULFILLMENT OF
THE REQUIREMENTS FOR THE DEGREE OF

MASTER OF SCIENCE

in

The Faculty of Graduate Studies and Postdoctoral Studies

(Physics)

THE UNIVERSITY OF BRITISH COLUMBIA

(Vancouver)

January 2017

Abstract

This thesis describes a method of using an ultra-cold ensemble of atoms confined in a trap as an atomic primary pressure standard. The development of the standard and its current status are described in detail. This standard uses a 3D MOT to trap ^{87}Rb and then transfer them to a quadrupole magnetic trap where the atoms undergoes collisions with a background gas. By measuring the number of atoms left in the magnetic trap as a function of time one extract a loss rate and from this rate determine the background gas density. This loss rate is a product of the density of the background, multiplied by the loss cross section averaged over the velocity distribution of the background gas. By computing the average loss cross section in the magnetic trap and measuring the loss rate, the density of the background gas can be determined. This gives a calibration free measurement of density of a background gas in the UHV range $(10^{-6} - 10^{-9})$ Torr or $(10^{-4} - 10^{-7})$ Pa which allows for it to be used as a standard. In conjunction with this, preparation of the atoms prior to the loss rate measurement is investigated to ensure accuracy and reproducibility of the standard. Finally a comparison between UBC's atomic standard and NIST's (National Institute for Standards and Technology) orifice flow standard is conducted via an ionization gauge which employed as a transfer standard. All measurement are carried out using Argon gas as the background gas of study.

Preface

This works in done in collaboration with James Fedchak of the National Institute of Standards and Technology in the USA. He supplied an ionization gauge and spinning rotor gauge. Chapter 3 and chapter 4 describes the all the data and results for the experiment. I was responsible for adding the magnetic trapping coil to the setup which was done with the help of Janelle Van Dongen. I added the RF coil system to the setup. I collected and analyzed all the data for this thesis. I also optimized and created the recipe for the experimental procedure. Fig. 3.1 and Fiq. 3.2 were adapted from the original produced by Janelle Van Dongen.

Table of Contents

List of Tables

List of Figures

Acknowledgements

I would like to thank Professor Kirk Madison and Dr. James Booth, for their guidance and supervision in the time that I have been in the lab. I would also like to thank Marisuz, Kahan, Koko, Gene, Will, William as I have been lucky enough to learn from them and a special thanks to Janelle Van Dongen for her guidance and patience in training me.

Dedication

To my parents

Chapter 1

Introduction

1.1 Motivation

The ability to measure and communicate physical properties is the essence of experimental science. The ability to quantitatively express these properties, requires the use of units. This makes defining a unit an essential part of experimental science. To define a unit one needs a standard. A standard is an artifact, system or process that defines units of measure and is the reference for other measurements. This thesis describes work to establish a new primary pressure standard using ultra-cold atoms. This new standard ties pressure or flux to the standard unit of time, the second.

Experiments with ultra-cold atoms have become a pillar in Atomic Molecular and Optical (AMO) physics, offering a variety of different physical phenomenon to explore. The field began with Ashkin's idea of using a laser to influence atoms and molecules using optical transitions[1]. Two years later in 1972 the first deflection of an atomic beam was produced[13]. Hansch and Schawlow proposed the use of light to manipulate atoms further by exploiting the Doppler effect to slow atoms down. By creating a velocity dependent radiation pressure on the atoms, one can slow atoms down to hundreds of micro-kelvins[12]. This reduction of the velocity of atoms using light can be seen as the beginning of laser cooling. From here the use of laser light with a magnetic field produced the first magneto-optical trap (MOT), allowing for the study of cold and localized atomic samples[22]. The ability to cool sample led scientists to investigate how cold they could make these atom clouds. The first lower limit was broken when sub-doppler cooling was achieved by using an optical molasses, scientists where were able to produce atomic ensembles at tens of micro-kelvin[18]. Evaporative cooling took temperatures down to hundreds of nano-kelvin pushing the lower limit of ultra-cold atoms further[21]. Cooling further and further led to the achievement of a Bose-Einstein Condensate (BEC) in atomic gases. The possibility of a BEC was first proposed by Bose and Einstein in 1924 and realized independently in 1995 by Ketterle and by Cornell and Wieman[7][2]. This achievement gave the field of ultra-cold atoms a lot of promise, by showing its capabilities

in simulating condensed matter systems and culminating in the 2001 Nobel prize[15][6]. The field went on to explore other areas of interest including placing atoms in an artificial lattice produced by laser light, phase transitions from different states of matter such as super-fluid to Mott insulators, as well as looking at strongly correlated systems[11]. Furthermore ultra-cold atoms have been proposed as quantum simulators and quantum computers[3][23].

Ultra-cold atoms have not only led to contributions in fundamental physics but have also enabled many advances in applied physics. Cold atoms offer a unique tool to physics - a physical system in which all of the quantum mechanical degrees of freedom can be controlled. This control makes cold atoms an excellent candidate for a measurement device. Cold atoms have and currently are being used to measure many different physical quantities ranging from electric and magnetic fields to gravitational fields and time. They allow for creation of devices with extraordinary sensitivity[16]. One of these devices is a cold atom based atomic clocks, in which frequencies of atomic transition can be measured with such high precision that it is the time standard across the world[5].

One area that ultra-cold atoms are poised to make a significant impact is in the area of pressure measurement. Pressure has been studied since antiquity, but it wasn't until recently that it has crossed paths with the field of AMO physics. The common method for measuring pressure in the ultra high vacuum range is with the use of ionization gauges. Ionization gauges use electrons boiled off a hot filament to ionize gas particles.

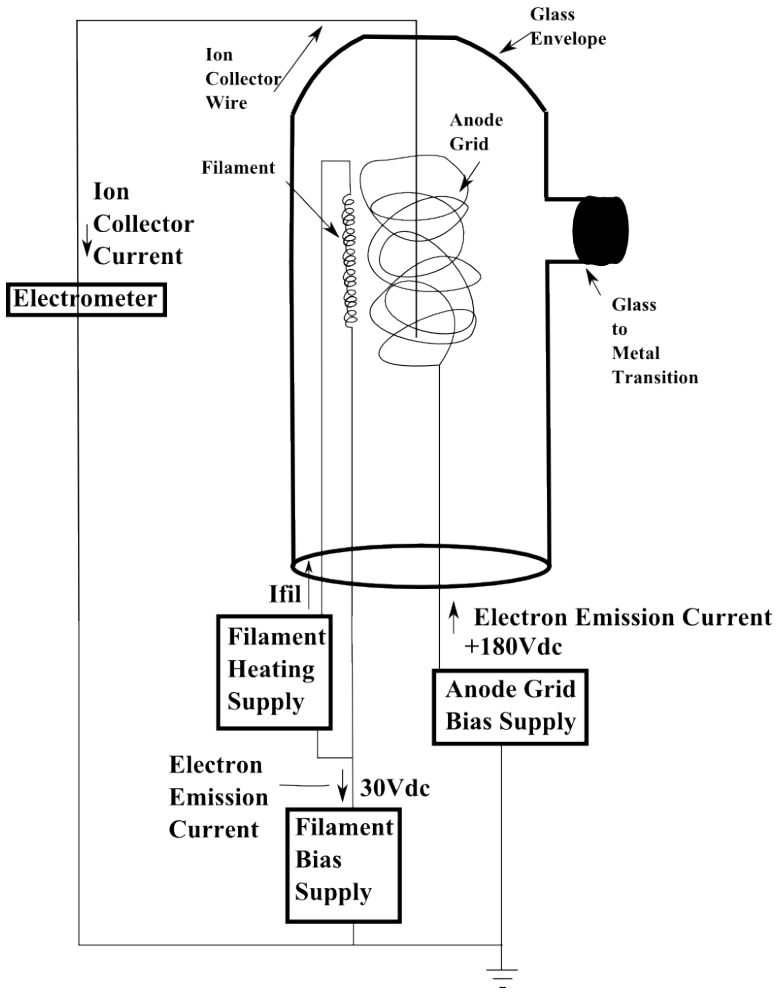

Figure 1.1: Schematic of a Bayard-Alpert ionization gauge. The gauge operates by boiling off electrons from the filament and having them accelerate towards the anode grid. As the electrons move through grid they ionize the atoms/molecules as they encounter them. If they do not encounter any gas, they continue along their path then exit the grid and are brought back due to the coulomb force. This results in multiple passes for the electrons through the gas in the detection volume.As ions are produced they are collected by the ion collector wire which results in a current that proportional to the pressure. This proportionality constant depends on the gauge temperature, the electron emission current, and the electric field within the gauge.

By collecting and counting these ions, and comparing this to the electron current, an indirect measure of the background pressure can be made. There are significant limitations of ionization gauges. First the ionization potential differs from species to species requiring a calibration for every type of gas measured. Second is that if these x-rays hit the ion-collector wire, they can produce electron emission resulting in a current that is indistinguishable from the current of arriving gas ions and the associated the pressure determination is confounded. For higher pressures a spinning rotor gauge is used to measure the pressure. It consists of a magnetized stainless steel ball that is spun up to a high rotation speed, and its deceleration is measured to determine the pressure.

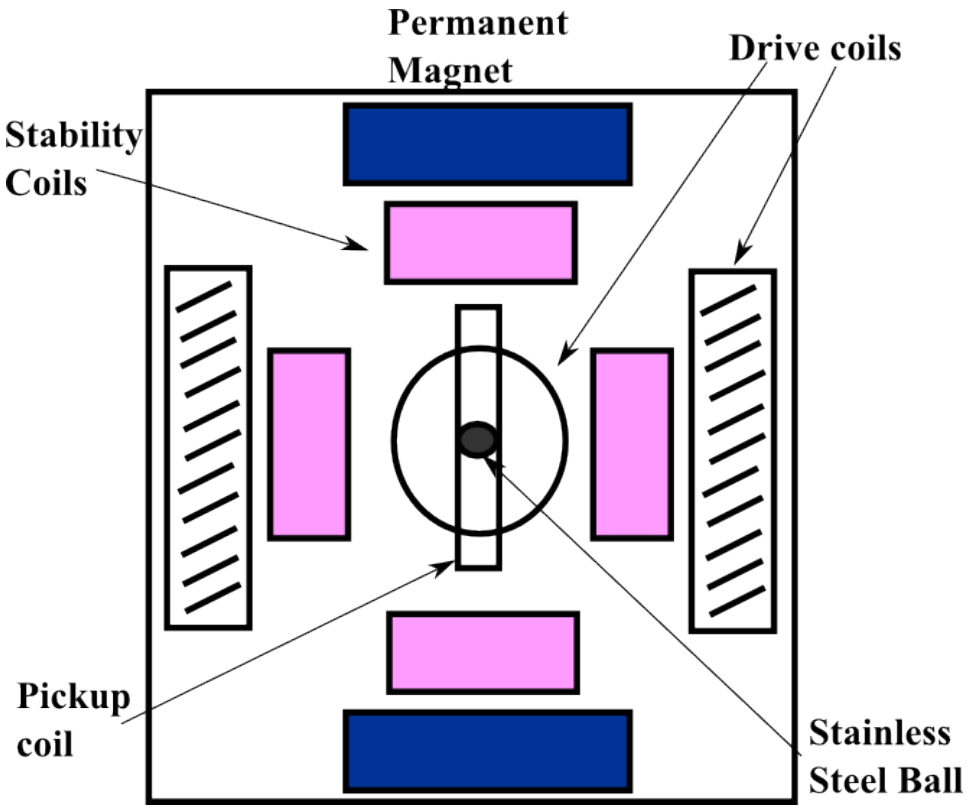

Figure 1.2: Cross section diagram of a spinning rotor gauge. It consists of; a pair of permanent magnets to suspend a stainless steel ball in the vacuum, pairs of stability coils to maintain orientation of the ball and drive coils to spin up the ball.

Finally both the ionization gauge and spinning rotor gauge need to be calibrated to a pressure standard to ensure the accuracy of the reading. For this purpose, pressure standards are maintained by standard laboratories all over the world.

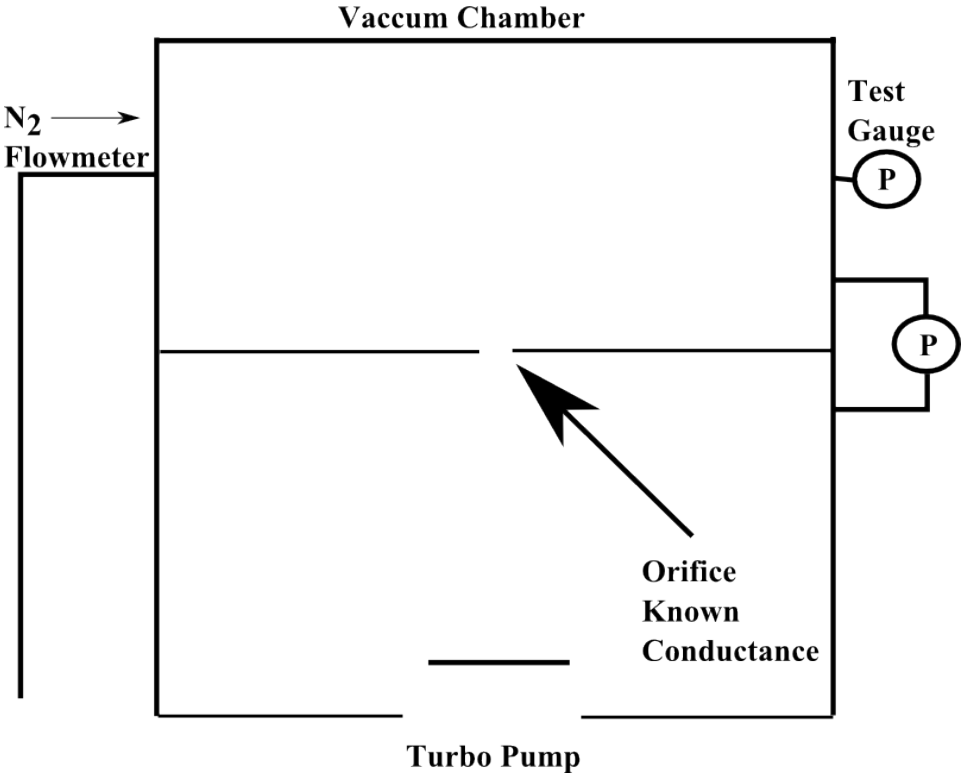

Figure 1.3: The orifice flow standard consists of two vacuum chambers separated by an orifice, which allows gas to flow from one chamber to the other. Gas enters with a constant volume flow rate through a flowmeter and exits through a turbo-molecular pump. Two gauges are attached to the side of the standard, one to measure the differential pressure in the two chambers, the other to be calibrated. There is a plate in the lower chamber to baffle the gas flow before it enters the turbo pump.

One type of vacuum pressure standard is an orifice flow standard such as the one at the US Nationals Institute of Standards and Technology (NIST). An orifice flow standard consists of two chamber attached by a small precisely machined orifice. Gas is flowed from the upper high pressure chamber

through the orifice to the lower low pressure chamber. By knowing the conductance of the orifice and the pressure ratio one can determine the pressure in the lower chamber. There a few issues with this type of system: First the out gassing of the chambers sets the base pressure that is attainable. Second, with lower pressure the assumption of a Maxwell-Boltzmann distribution of the gas, one of the crucial assumptions for proper operation becomes invalid. For these reason a new standard is needed, especially for lower pressure operation.

Ultra-cold atoms offer an alternative to the current pressure standard since pressure can be measured by the collisions between sensor atoms and the atoms or molecules in the background gas. Thus, by studying the interaction physics between trapped atoms and background gases one can devise a new pressure standard. This new standard is thus based on fundamental and immutable laws of nature and relies only on the knowledge of the long-range interaction potential between the trapped atom and the colliding particle.

1.2 Thesis Overview

This thesis describes progress towards the realization of this new standard and is organized in the following manner: chapter 2 begins by describing the physical basis of the two types of atom traps being used, a magneto-optical trap (MOT) and a magnetic trap (MT), and includes a discussion of the scattering theory for collision of Ar onto Rb. The chapter ends with a discussion of the trapping potential of the MT. In Chapter 3, the experimental setup is discussed including our use of a 2D MOT for loading a 3D MOT to allow for low pressure experiments. We also discuss the trapping coils for the MT, the RF-knife used to set the trap depth, and details of the optics used. Chapter 3 also describes the various methods for preparing the atoms before the loss rate measurement is performed. These preparation steps include cooling and optically pumping the atoms and then preparing the energy distribution in the MT using an RF-knife to remove the most energetic atoms. Chapter 4 goes on to discuss the results of the experiment; atom number measurements as a function of time, loss rate measurements as a function of argon pressure and finally the measure of the gas calibration factor the ionization gauge. The future work is proposed in chapter 5 were measurements of other noble gases and nitrogen are recommended. Measurements of gas mixtures are discussed as they offer an opportunity to explore the residual gas analysis capabilities that the cold atom gauge could

offer. Finally cross section measurements of different Rydberg states could be measured.

Chapter 2

Theory

In this chapter, we discuss various aspects of the theoretical basis of this work. The topics include laser cooling, magnetic trapping, and the physics of collisions. We focus on the details of the MOT and magnetic trap that are relevant to pressure measurements as well as how the loss rate is determined from a quantum scattering calculation.

2.1 Magneto-Optical Traps

Magneto-Optical traps (MOTs) are the starting point of the experiment. They capture atoms from the background vapour and produce the cold sensor ensemble. Here we discuss three aspects of MOTs relevant for their use for pressure measurements. These topics are the mechanism for cooling (Doppler cooling) and the typical ensemble temperature in the MOT, the loading dynamics of a MOT, and methods for measuring the atom number in the MOT. An understanding of these processes is required for precise and accurate pressure sensor measurements.

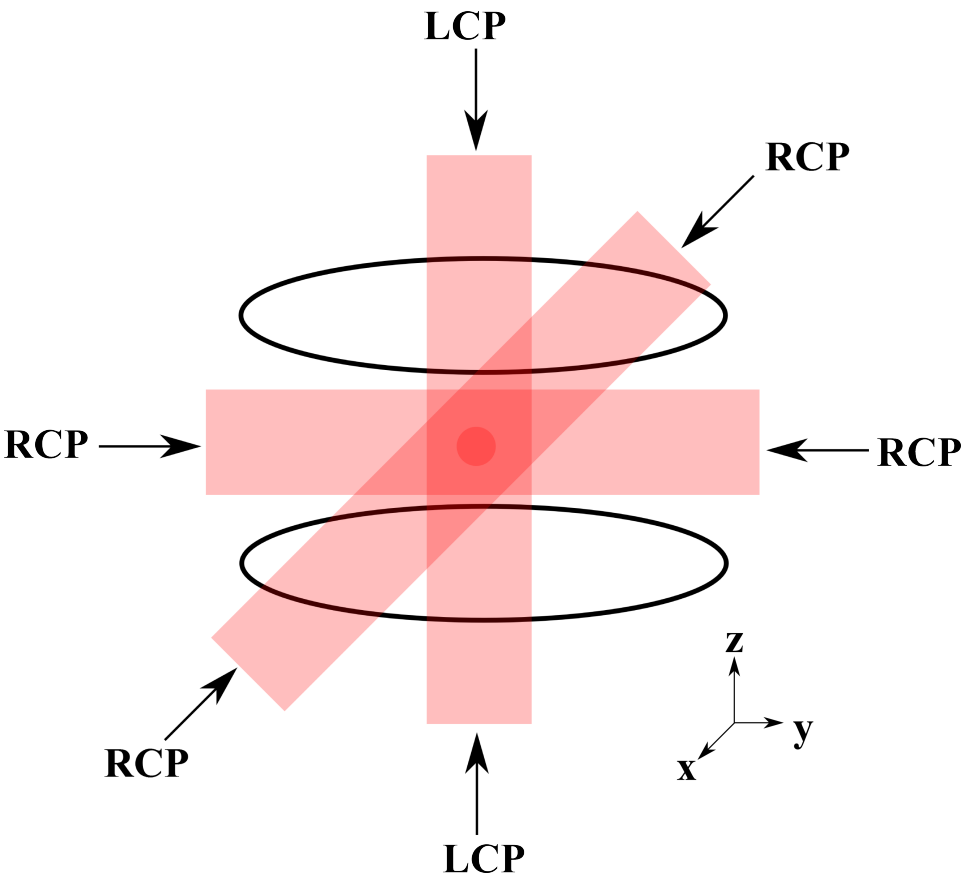

Figure 2.1: This is a pictorial representation of a MOT. The MOT consists of six counter propagating laser beams, a pair along each orthogonal spatial axis. Each pair has a certain polarization to ensure that the correct atomic transition is driven. On the x and y axes, we have right circularly polarized (RCP) light and on the z axis we have left circularly polarized (LCP) light. A pair of anti-Helmholtz coils are also used to create the magnetic field required for the trap. Due to the fact that the magnetic field directions are in the opposite directions for x and y as opposed to z leads to the need for the opposite polarization along z.

2.1.1 Doppler Cooling

One mechanism of slowing atoms in a MOT is Doppler cooling. It involves using off resonance light to slow down a moving atom, reducing its kinetic

energy. The idea can be illustrated in 1D by placing an atom in between two counter propagating laser beams. The force that each beam exerts on the atom in the low intensity limit, in which the intensity of the laser I is small compared to the saturation intensity I_{sat} can be described by the following where $(I < I_{sat})$[20];

$$F_{\pm} = \frac{\hbar\vec{k}\gamma}{2}\frac{s}{1+s+[2(\delta\mp kv)/\gamma]^2} \tag{2.1}$$

Here s is I/I_{sat}, γ is the linewidth of the transition and δ is the detuning from resonance. Now considering the two laser beams, the total force from them up the first order in v is[20]

$$F = 4\hbar\vec{k}^2\frac{s\delta v}{\gamma(1+s+4\delta^2/\gamma^2)^2} \tag{2.2}$$

If the light is tuned below resonance then this force can appear as a velocity dependent dissipative force. This can be expressed in terms of a damping coefficient, β.

$$F = -\beta v \tag{2.3}$$

Looking at the energy we find that the light acts as a dissipative mechanism, removing kinetic energy from the atom according to Eq. 2.4.

$$\dot{E} = -\beta v^2 \tag{2.4}$$

By using six beams, a pair along each orthogonal coordinate axis, one can reduce the velocity of the atom very near to zero, producing an optical molasses. In experiments a zero velocity is never achieved, this is due to residual heating from photon re-emission occurring in all directions. A lower limit is achieved when $|\delta| = \gamma/2$

$$k_B T = \frac{\hbar\gamma}{2} \tag{2.5}$$

This limit is called the Doppler-cooling limit[20]. While there are other cooling mechanisms in the MOT that can lead to temperatures below the Doppler cooling limit, this limit is nevertheless a good estimate of the temperature of the atoms in the MOT[20]. This residual thermal motion of the atoms is important to keep in mind since it limits the temperature of the atoms when transferred into a magnetic trap and leads to a reduction of the momentum gain required to escape the trap due to the non-zero initial kinetic energy.

2.1.2 Loading Dynamics

The loading dynamics of a MOT play an important role in the application of a MOT for pressure measurements. The loading dynamics of a MOT can be modeled by

$$\dot{N} = R - \Gamma N - \beta \int n^2(\vec{r}, t) d^3\vec{r} \tag{2.6}$$

The loading rate R is the number of atoms entering the trap per second, ΓN is the loss rate due to collisions with atoms in the background and $\beta \int n^2(\vec{r}, t) d^3\vec{r}$ encompasses losses due to radiative escape, fine-structure collisions, hyperfine collisions, intra-trap collisions and is dependent on the density of the atoms in the MOT , n(r,t). The solution to this differential equation is examined in two limiting regimes that a MOT can reach. The first regime is the constant volume regime. The constant volume regime is one in which the MOT cloud is dilute enough that atom-atom repulsive interactions from light rescattering are negligible and atoms are confined in a spatial volume of fixed size. In this regime, the MOT grows in number with a constant volume. However, once the density of the MOT is high enough, repulsive forces between the atoms cause the MOT to grow in volume with increasing number such that the peak density does not change. The constant volume regime can be modeled by assuming the atomic density has a Gaussian profile $n(\vec{r}) = n_0 e^{-\frac{r^2}{2w^2}}$ where n_0 is the peak density at the center of the trap $\vec{r} = 0$ and w is the width (assumed here to be a constant). This allows Eq. 2.6 to be written as;

$$\dot{N} = R - \Gamma N - \beta w (2\pi)^{\frac{3}{2}} N^2 \tag{2.7}$$

Solving this equation results in[8]

$$N(t) = \frac{R}{\Gamma + \beta n'} \left(\frac{1 - e^{-(\Gamma - 2\beta n')t}}{1 + \chi e^{-(\Gamma - 2\beta n')t}} \right) \tag{2.8}$$

Where χ equals $\frac{\beta n'}{\Gamma + \beta n'}$ and

$$n' = \left(\frac{\int n^2 d^3 r}{\int n d^3 r} \right) \tag{2.9}$$

is the average steady state density.

With a sufficiently large population the MOT will enter the constant density regime. Applying the constant density condition to Eq. 2.6 results in the follow,

$$\dot{N} = R - \Gamma N - \beta \overline{n} N \tag{2.10}$$

The solution to the above differential equation is

$$N(t) = \frac{R}{\Gamma + \beta\overline{n}}(1 - e^{-(\Gamma+\beta\overline{n})t}) \tag{2.11}$$

Aside from understanding the changing behavior of the 2-body losses in the MOT, understanding these regimes is useful for loading atoms into the MT. As the MOT is filled and enters the constant density regime, the number of atom per volume in the center of the trap begins to reach a constant. This constant density allows the transfer of an exact number of atoms to the MT from the MOT if a certain central volume is selected.

2.1.3 Atom Number Calibration

Counting the number of atoms left in the MOT or the MT trap is the main measurement of the experiment. Therefore, the ability to accurately and precisely measure the atom number is of utmost importance. There are two main methods of measuring the atom number in a trap. The first method involves the fluorescence measured on a photodiode which is directly related to the number atoms. This relationship is seen through Eq. 2.12 where the measured photodiode voltage (V) is related to the atom number (N) , the scattering rate (Γ) and a conversion parameter (α). The parameter α takes into account the transfer efficiency of a photon emitted by a single atom to the voltage measured after the amplified photodiode.

$$V = \alpha\Gamma N \tag{2.12}$$

$$\Gamma = \frac{\gamma}{2}\frac{I/I_{sat}}{1 + I/I_{sat} + \left(\frac{2\Delta}{\gamma}\right)^2} \tag{2.13}$$

The fluorescence method requires measuring both the scattering rate of the atoms and α, the conversion parameter. This measurement can be made, however it requires a more elaborate procedure[**?**]. These issues can be avoided by using a different technique called, optical pumping. Optical pumping involves using a separate beam to optically pump atoms from one state to another and measuring the photon loss[4]. For ^{87}Rb, atoms start in the $F = 2$ state where they are pumped to the excited state $F^{'} = 2$. Following this excitation, the atoms relax into either the $F = 2$ or $F = 1$ ground state by the emission of a photon. By measuring the number of photons required to transfer all the atoms into the $F = 1$ state, and knowing

the average number of photons needed to pump a single atom into the $F = 1$ state, one can determine the atom number by the following formula

$$N = \frac{A}{\phi h\nu} P \tag{2.14}$$

where A the integrated attenuation of the voltage signal, ϕ the average number of photon scatter per atom , $h\nu$ the photon energy, P the optical power to the photodiode. By taking multiple measurements of various atom numbers using optical pumping and their corresponding fluorescence voltages, the relation between voltage and atom number can be determined. The most important outcome of such a comparison of the atom number as determined by optical pumping and by fluorescence is to verify that the fluorescence signal is linear in the atom number. Linearity of the signal is absolutely key to a correct determination of the loss rate and corresponding pressure.

2.2 Magnetic Traps

Alongside the MOT, the MT is the main trap used to study the collisions of the trapped particles and colliding background gas. The magnetic trap is created by a pair of coils in an anti-Helmholtz configuration, seen in Fig. 2.2. This type of trap is the simplest kind that one can use to trap atoms. This quadrupole magnetic trap has a zero field at the center and a linearly increasing field away from the center. The magnetic field to first order in the axial and radial direction is,

$$B_z = 3\mu_0 \frac{DR^2}{(D^2 + R^2)^{5/2}} Iz \tag{2.15}$$

$$B_\rho = \frac{3}{2}\mu_0 \frac{DR^2}{(D^2 + R^2)^{5/2}} I\rho \tag{2.16}$$

Thus, the resulting field has twice the gradient in the axial direction compared to the field in the radial direction. The field gradient creates a spatially confining force that will trap the atoms in a particular hyperfine state.

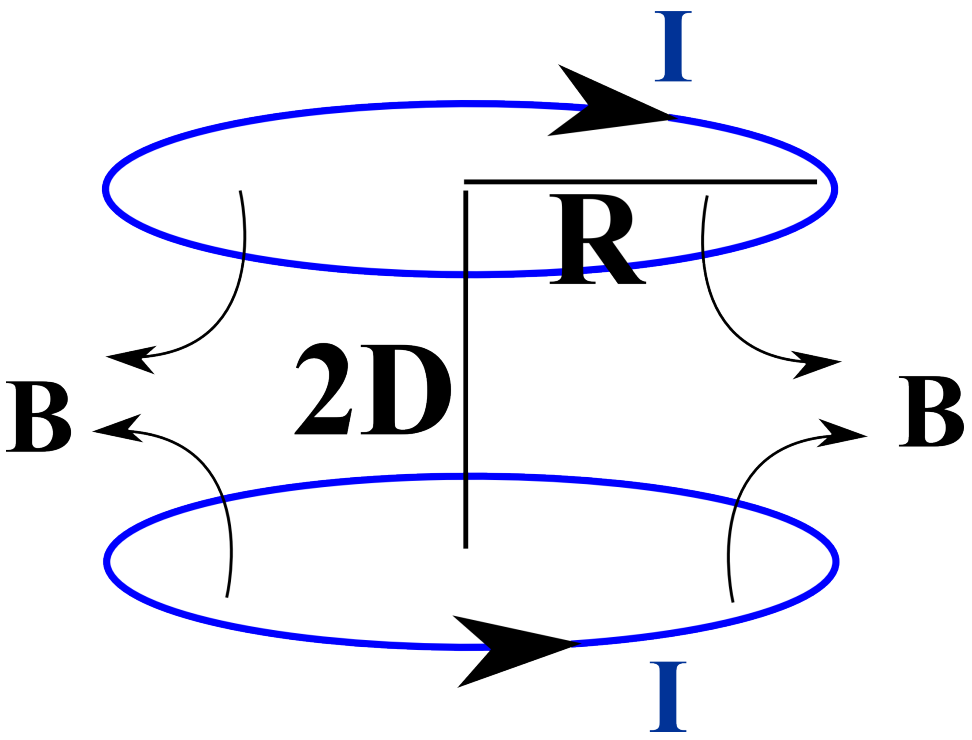

Figure 2.2: Magnetic field lines generated by pair of anti-Helmholtz coils used to produce the field for the magnetic trap.

As the atoms move in the magnetic trap, their magnetic potential energy varies with spatially varying magnetic field. This potential energy is different for the different atomic hyperfine energy levels: some levels are trapped (diamagnetic states) while others are not (paramagnetic) states. Atoms will stay trapped as long as the local magnetic field doesn't change too rapidly as the atoms move. The potential energy that the atoms experience is

$$U(r) = m_F \mu_B g_F |B(r)| \tag{2.17}$$

where m_F is the hyperfine state magnetic sub-level, μ_B is the Bohr magneton and g_F is the Landé g-factor which is -1/2 for the F=1 ground state of ^{87}Rb.

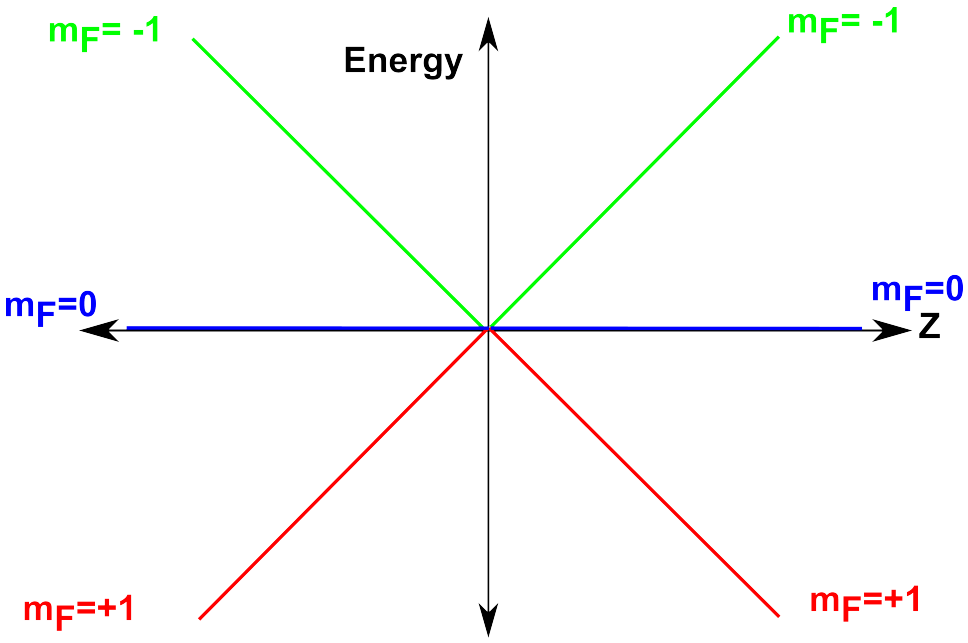

Figure 2.3: The energy splitting of the different sub-levels for the ground state $F = 1$ as a function of position. In the absence of a magnetic field these levels are degenerate.

2.2.1 Gravitational Sag

The magnetic potential is not the only potential that influences atoms in a magnetic trap. Gravity also plays an important role. Fig. 2.4 shows the potential energy that the atoms experience including gravity. This shift is a result of the gravitational field present along the vertical symmetry axis of the B-field.

$$U_{\text{potenital}} = U_{\text{Zeeman}} + U_{\text{Gravity}} \tag{2.18}$$

$$U_{\text{potenital}} = -\vec{\mu} \cdot \vec{B}(\vec{r}, I) + mgz \tag{2.19}$$

The potential energy is now modified and this leads to two main effects: First, the asymmetrical trapping potential can lead to an anisotropic trap depth, second, a minimum B-field gradient is required to overcome the gravitational force, which would otherwise cause the atoms to drop out of the trap. The trapping asymmetry can be seen where the atom below the zero

position ($\vec{r} = 0$ which coincides with zero of the B-field) have a lower barrier of escape, while atoms above the zero position see a barrier higher than that produced by the magnetic field alone.

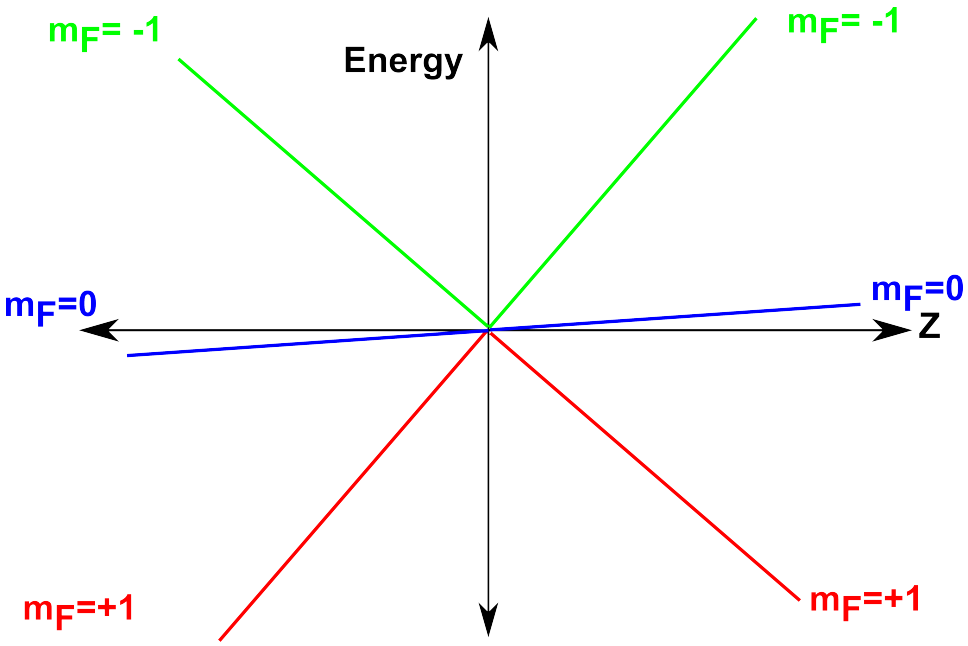

Figure 2.4: Energy level structure of the $F = 1$ states in the presence of gravity. Gravity causes an asymmetry in the trap potential that leads to an anisotropic trap depth.

2.2.2 Gravitational Filtering

The presence of gravity appears as an issue for magnetic traps, however, one benefit it offers is gravitational filtering. Gravitational filtering uses the fact that different magnetic sub-levels have different potential energy surfaces in the same B-field. Eq. 2.17 shows that the $m_F = 2$ requires half the field strength than the $m_F = 1$ to achieve the same magnetic potential energy. Thus, there is a magnetic field gradient at which $m_F = 2$ state is trapped but $m_F = 1$ is not.

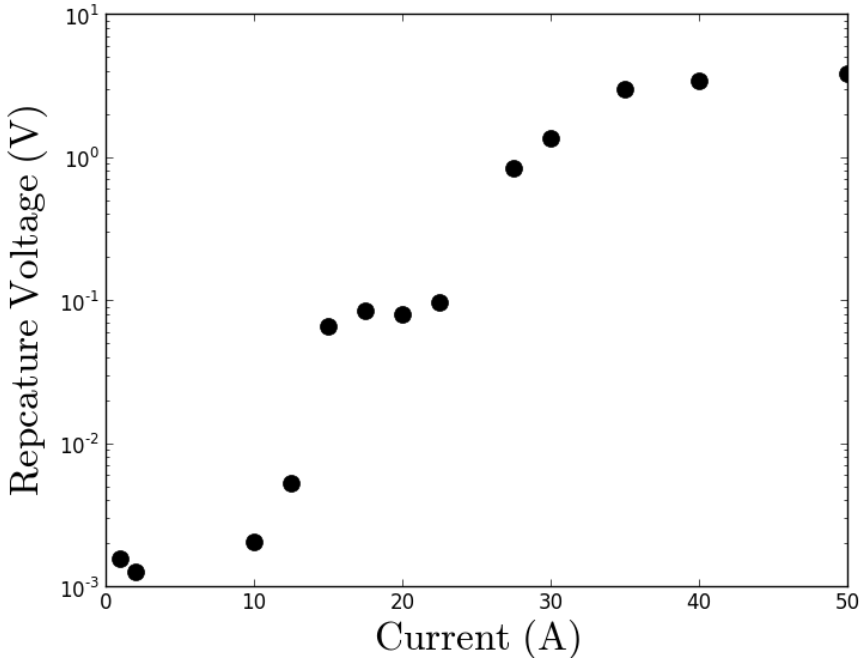

Figure 2.5: Plot of recapture voltage in the MT vs. the current of the MT. The plot shows that for current below 11.2 A there is no recapture in the MT. This is because the the magnetic force of the MT is not enough to overcome gravity for any atomic states. As the current is increased past 11.2 A there appears to be some recapture in the MT and then a leveling off, this signal is of the $m_F = 2$ state. As the current is increased past 22.4 A the recapture signal increases again and levels off, this signal is of the $m_F = 1$ state which requires twice as much current as the gradient is now able to support atoms in either the $mF = 2$ or the $mF = 1$ hyperfine sublevels. As expected, the threshold currents scale as the mF value..

The difference in potential energy allows for the magnetic state purification through the use of gravity as a filtering process. One limitation of this method is a lengthy waiting period for filtration. In our setup, we must wait 70 ms for the atoms in the un-trapped spin state to fall out of the MOT recapture region.

2.2.3 Majorana Losses

Quadrupole Magnetic traps are a convenient tool for trapping atoms. However, one issue with this type of trap is a zero field in the center. This zero field point can lead to atoms not having an axis of quantization to follow, resulting in loss from the trap. This loss is called spin flip loss or Majorana loss. These spin flips, as the name suggests, occur when atoms pass through the center of the magnetic trap and experience an abrupt change in the magnetic field direction. This abrupt change leads to the possibility of flipping from a trappable state to an untrappable one. The condition for a spin flip involves the local change in the magnetic field to be larger than the atom's Larmor frequency. Mathematically the loss rate due to spin flips can be estimated by the follow equation[21]

$$\Gamma_{\text{Majorana}} \approx \frac{\hbar}{ml^2} \tag{2.20}$$

where l is the radius of the cloud and m is the mass of the atom. We can express this condition in terms of the magnetic field gradient B' and the temperature as [19]

$$\Gamma_{\text{Majorana}} \approx \frac{\hbar}{m}(\frac{\mu B^{'}}{k_B T})^2 \tag{2.21}$$

where $B^{'}$ is the local gradient of the magnetic field. These equations allow for the estimate of the losses due to spin flips, if we take T to be $150\mu K$ and $B^{'}$ to be $99\frac{G}{cm}$ then $\Gamma_{Majorana}$ is 40 seconds. The long lifetime ensures that spin flips will will not dominate the pressure measurements for pressures above 10^{-11} Torr .

2.2.4 Magnetic Trap Depth

The magnetic trap depth is defined by the energy the atoms must have to escape the trap and be lost. One method for setting the trap depth in a magnetic trap involves using a RF coil. The RF coil produces an oscillating B-field which can couple adjacent magnetic sub-levels in the trap and allow for magnetic dipole transitions ($\Delta m_F = \pm 1$). By driving transitions from trappable to untrappable states, the RF radiation can be used to set the maximum value of the energy distribution of the atoms alongside fixing the trap depth. The potential energy of atoms inside the magnetic trap is given by

$$U_{\text{Zeeman}} = -\vec{\mu} \cdot \vec{B} = \mu_B g_F m_F b I \sqrt{\frac{x^2}{4} + \frac{y^2}{4} + z^2} \tag{2.22}$$

where bI is the magnetic field gradient $\left(\frac{\partial B}{\partial z}\right)$ along the z-axis. Adding the gravitational potential energy results in

$$U_{\text{potenital}} = \mu_B g_F m_F bI \sqrt{\frac{x^2}{4} + \frac{y^2}{4} + z^2} + mgz \tag{2.23}$$

The application of an RF signal to the atoms in a gravity free situation produces a transition between trapped and untrapped states on the surface of an ellipsoid specified by the locus of points x_d, y_d, and z_d satisfying Eq. 2.24. As atoms travel in the magnetic trap and pass a certain point in space, they interact with the RF field and may spin flip from a trappable state to an untrappable one. This interaction surface traces out an ellipsoid, therefore it is named the "ellipsoid of death".

$$\Delta U_{\text{Zeeman}} = \pm \mu_B g_F bI \sqrt{\frac{x_d^2}{4} + \frac{y_d^2}{4} + z_d^2} = h\nu \tag{2.24}$$

Atoms that do not possess enough energy to reach the "ellipsoid of death" remain in the trap. By tuning the RF frequency, the volume and the potential energy the atoms occupy can be controlled. Atoms that reach the surface are lost from the trap, setting the upper limit on the potential energy to be the following:

$$U_{\text{limit}} \leq \mu_B g_F m_F bI \sqrt{\frac{x_d^2}{4} + \frac{y_d^2}{4} + z_d^2} + mgz \tag{2.25}$$

In order to find the points where the transitions occurs, it is useful to derive the minimum current required to create the field gradient that can support the atoms against gravity. This current is when the gravitational force equals the Zeeman force.

$$|\vec{F}_g| = |\vec{F}_{Zeemam}| \tag{2.26}$$

$$\frac{mg}{bI_0} = \mu_B g_F |m_F| \tag{2.27}$$

where I_0 is the minimum current and equal to 22.4 A in our setup. This provides the useful relationship

$$\mu_B g_F b = \frac{mg}{m_f I_0} \tag{2.28}$$

Combing Eq. 2.25 and Eq. 2.27 we have

$$U_{\text{limit}} \leq mg\frac{I}{I_0}\sqrt{\frac{x_d^2}{4}+\frac{y_d^2}{4}+z_d^2}+mgz \tag{2.29}$$

where

$$z_d = \frac{h\nu|m_F|I_0}{mgI} \tag{2.30}$$

for the z-axis and for the x and y

$$x_d = \frac{2h\nu|m_F|I_0}{mgI} \tag{2.31}$$

$$y_d = \frac{2h\nu|m_F|I_0}{mgI} \tag{2.32}$$

Gravity modifies the trapping potential and the minimum potential the atoms encounter along the z direction.

On the z-axis the potential becomes

$$U_{z,\text{limit}} \leq mg\frac{I}{I_0}z_d + mgz_d \tag{2.33}$$

By re-writing the expression in terms of the RF energy we have

$$U_{z,\text{limit(min)}} \leq h\nu|m_F|(1-\frac{I_0}{I}) \tag{2.34}$$

$$U_{z,\text{max}} \leq h\nu|m_F|(1+\frac{I_0}{I}) \tag{2.35}$$

$$U_{x,y,\text{limit}} \leq h\nu|m_F| \tag{2.36}$$

The anisotropy introduced by the gravitational field is clearly illustrated by Eq. 2.34 and Eq. 2.35. The consequence of which is if atoms have enough time to explore the entire trap they will encounter the minimum in the z - direction.

$$U_{z,\text{limit}} \leq h\nu(1-\frac{I_0}{I}) \tag{2.37}$$

By using the RF knife to eject atoms at a specific energy, tailoring of the energy distribution can be achieved. Furthermore by setting the RF knife to interrogate a range of frequencies from the trap depth and above, atoms with higher energies will efficiently be removed.

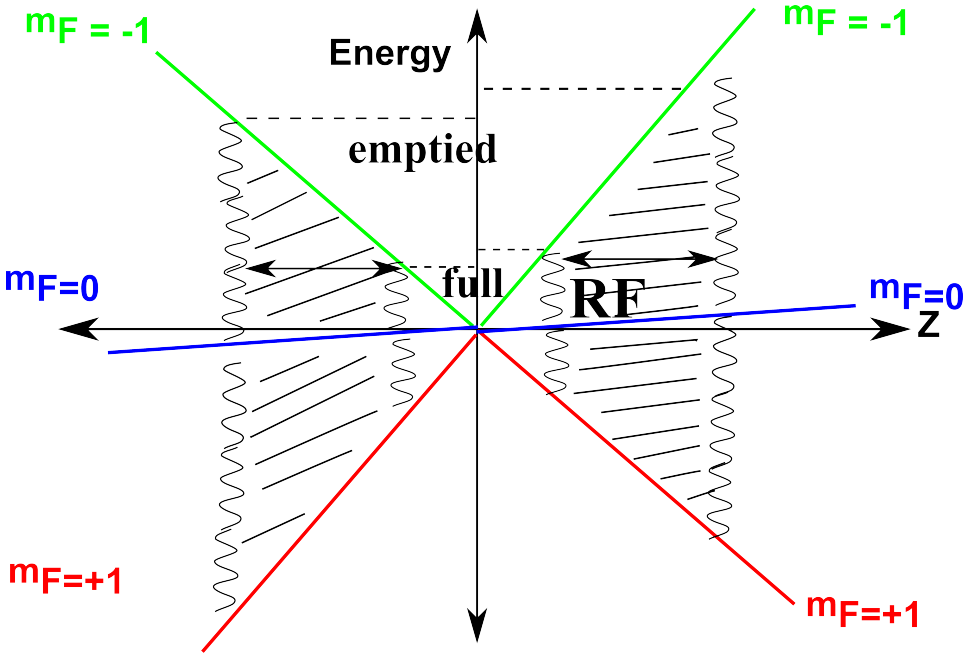

Figure 2.6: This figure shows the coupling of the different magnetic subslevels to each through a radio-frequency signal. This signal is swept from high to low frequencies to eject atoms out of the trap within a range of potential energies. This RF signal can thus be used to prepare the sensor ensemble by removing atoms above a certain energy.In the presence of gravity the potential energy of the atoms are asymetric in space pushing the atoms towards a non-zero point as a potential energy minimum. This shift causes a spatial and energy asymmetry to the atomic distribution in the magnetic trap.

2.3 Elastic Scattering theory

The topic of particle-particle scattering is ubiquitous in ultra-cold physics. It is the mechanism behind the thermalization of quantum gases and a loss mechanism in traps. Here scattering is examined in the context of elastic scattering of particles at large relative velocities.

2.3.1 Two Body Problem

The simplest scattering model is a two-body collision between two particles that interact through a potential. The Hamiltonian of the system is

$$H = \frac{\vec{p}_1^2}{2m_1} + \frac{\vec{p}_2^2}{2m_2} + V(|\vec{r}_1 - \vec{r}_2|) \tag{2.38}$$

and includes three terms; the first two terms are the kinetic energy terms of each particle and the third is the potential energy of interaction. This problem can be solved in the center of mass frame. To change to the center of mass frame a few new variables are needed. These include; total mass M, total momentum P, and relative position r, relative momentum p and reduced mass μ

$$M = m_1 + m_2 \tag{2.39}$$

$$\vec{P} = \vec{p}_1 + \vec{p}_2 \tag{2.40}$$

$$\vec{r} = \vec{r}_1 - \vec{r}_2 \tag{2.41}$$

$$\vec{p} = \mu(\vec{v}_1 - \vec{v}_2) \tag{2.42}$$

By making the substitution the Hamiltonian becomes;

$$H = \frac{\vec{P}^2}{2M} + \frac{\vec{p}^2}{2\mu} + V(\vec{r}) \tag{2.43}$$

The Hamiltonian now describes a particle moving with mass M and one with the reduced mass μ describing the relative motion of the particles. By working in the center of mass frame, the momentum of the center of mass in the Hamiltonian becomes a constant, reducing Eq. 2.43 to

$$H^{'} = \frac{\vec{p}^2}{2\mu} + V(\vec{r}) = H - H_{CM} \tag{2.44}$$

This picture gives a single particle of mass μ moving in a potential $V(\vec{r})$

2.3.2 Scattering Cross Section

We now wish to describe the calculation of the scattering cross section. We begin with the Schrodinger equation

$$\left(\frac{\vec{p}^2}{2\mu} + V(\vec{r})\right)\psi_k(r) = E_k\psi_k(r) \tag{2.45}$$

and the ansatz

$$\psi_k(r) = \psi_{inc}(r) + \psi_{sc}(r) \tag{2.46}$$

which includes an incident wave $\psi_{inc}(r) \propto e^{i\vec{k}\cdot\vec{r}}$ and scattered wave. The scattered wave can be found by investigating certain symmetries. For potentials falling off faster that r^{-2} and as r $\to \infty$, the solution for the scatter wave is of the form

$$\psi_{sc}(r) = f(k,\theta,\phi)\frac{e^{ikr}}{r} \tag{2.47}$$

where $f(k,\theta,\phi)$ is the scattering amplitude, which depends on k, the wavevector of the incoming particle and θ,ϕ the direction of scattered wave. If the potential is isotropic the Schrodinger equation is re-written in terms of the spherical coordinates and the angular momentum operator as [17]

$$\frac{\hbar}{2\mu}\left(-\frac{1}{r^2}\frac{\partial}{\partial r}\left(r^2\frac{\partial\psi_r}{\partial r}\right)+\frac{\hat{L}^2}{r^2}\psi_r\right)+V(r)\psi_r = E\psi_r \tag{2.48}$$

where V(r) has no angular dependence. The wavefunction can now also be separated in terms of a radial and an angular part.

$$\psi_r(r,\theta,\psi) = R_l(r)Y_l,m(\theta,\phi) \tag{2.49}$$

Substituting this wavefunction into the Schrodinger equation leaves us with

$$\frac{1}{r^2}\frac{d}{dr}\left(r^2\frac{dR_l}{dr}\right)-\frac{l(l+1)}{r^2}R_l+\frac{2\mu}{\hbar^2}\left(E-V(r)\right)R_l = 0 \tag{2.50}$$

The scattering problem is cylindrically symmetric along ϕ, allowing us to change ψ from spherical harmonics to Legendre polynomials, leaving it in this new form

$$\psi(r,\theta) = \sum_{l=0}^{\infty}(2l+1)i^l e^{i\delta_l}R_l(kr)P_l(cos\theta) \tag{2.51}$$

By re-expressing the radial part of the solution R_l in terms of $\psi_l = krR_l(r)$ we have[17]

$$\left(\frac{d^2}{dr^2}+W(r)\right)\psi_l(r) = 0 \tag{2.52}$$

where

$$W(r) = k^2 - 2\frac{\mu}{\hbar^2}V(r) - \frac{l(l+1)}{r^2} \tag{2.53}$$

By setting up a new differential equation

$$y'(r) + y^2(r) + W(r) = 0 \tag{2.54}$$

where

$$y_l(r) = \frac{\psi_l'}{\psi_l} \tag{2.55}$$

and

$$\psi_l(r) = \cos(\delta_l)\left(krj_l(kr) - K_l(k)krn_l(kr)\right) \tag{2.56}$$

solving for K_l is achievable[14].

The scattering amplitude can also be expressed in terms of Legendre Polynomials as

$$f(k,\theta) = \frac{1}{k}\sum_{l=0}^{\infty}(2l+1)e^{i\delta_l}\sin(\delta_l)P_l(\cos(\theta)) \tag{2.57}$$

where δ_l is the phase shift for the l^{th} partial wave and is related to the T-matrix

$$T_l(k) = e^{i\delta_l}\sin(\delta_l) \tag{2.58}$$

The T-matrix can solved from the S-matrix

$$S_l(k) = e^{2i\delta_l} = 1 + 2iT_l(k) \tag{2.59}$$

which in turn needs the K-matrix

$$S_l(k) = \frac{1 + iK_l(k)}{1 - iK_l(k)} \tag{2.60}$$

$$K_l(k) = \tan\delta_l(k) \tag{2.61}$$

In this work, a Lennard-Jones potential is used to model the interaction potential to solve for the K-matrix. It is a potential which describes an induced dipole-dipole interaction between colliding particles. Its long range interaction is modeled by a r^{-6} and we model the short range repulsive part as a r^{-12}.

$$V(r) = \frac{C_{12}}{r^{12}} - \frac{C_6}{r^6} \tag{2.62}$$

By using numerical methods the solution for $y_l(r)$ can be obtained. What is required for this process is the potential and the reduced mass. The solution allows for the K-matrix to be found which gives the T-matrix, from which the total elastic cross section can found.

$$\sigma = \frac{4\pi}{k^2}\sum_{l=0}^{\infty}(2l+1)|T_l(k)|^2 \tag{2.63}$$

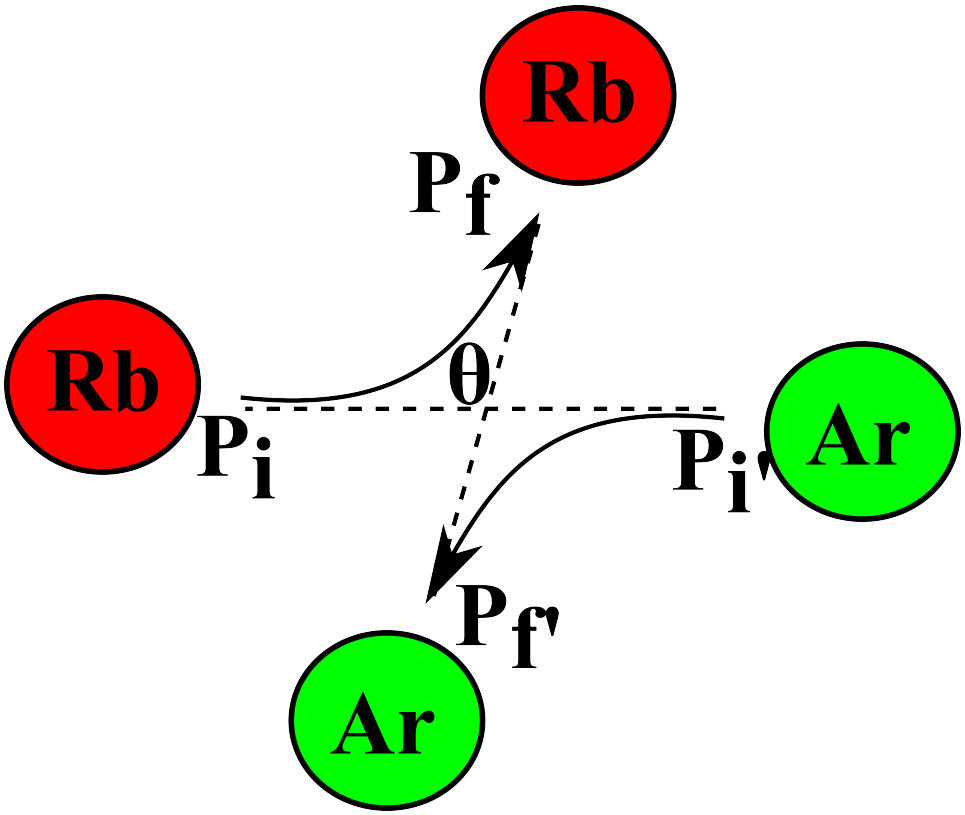

Figure 2.7: This figure shows the an elastic collision in the center of mass frame between Ar and Rb showing their initial and final momentum states.

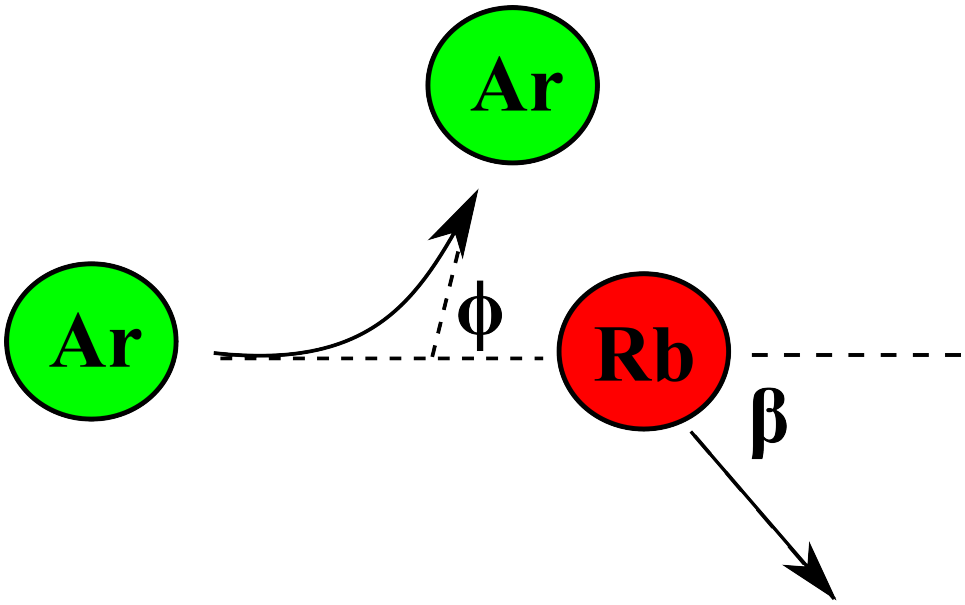

Figure 2.8: In the lab frame a collision can be seen with the Rubidium appearing stationary and the Argon atom moving towards it. As the Argon passes the Rubidium atom it does so traveling off at an angle, this angle can be used to parametrize the momentum transfer from the Argon atom to the Rubidium atom. Angles that are above a certain threshold result in a momentum transfer large enough to induce loss from the trap, while angles that are below result in heating. This threshold (minimum angle) is directly related to the trap depth. This threshold is set by the minimum energy needed to escape the trap.

2.4 Loss Rate

Background collisions are an undesirable phenomenon in ultracold systems, limiting both the signal integrity (e.g. in atomic clocks) and lifetime of a cold ensemble. In this work this undesirable effect is utilized to better understand the composition of the background gas in the vacuum system. The loss rate of atoms in a MT can be expressed as

$$\Gamma = \sum_{i}^{N} n_i \langle \sigma_{\text{loss}} v_i \rangle_{(Rb,i)} \tag{2.64}$$

where the loss rate, Γ, is the sum over the background species of density n_i, multiplied by the loss cross section σ_{loss} and relative velocity v, of the background gas. The brackets represent an average taken over the velocities of a Maxwell-Boltzmann distribution. This $\langle \sigma v \rangle$ term quantifies the interaction of the trap atoms and colliding background particles. The interaction is not only species dependent but also depends on the depth of the trapping potential demanding that the dependencies be explored. The transfer of energy from the background particle to the trapped particles (assuming the trapped particle initially has no kinetic energy) is[10]

$$\Delta E = \frac{\mu^2}{m_t} |\vec{v_r}^2| (1 - \cos(\theta)) \tag{2.65}$$

Here the energy transfer depends on the reduced mass μ, the relative velocity $\vec{v_r}$, mass of the trapped particle m_t and the center of mass frame collision angle θ. By rearranging the equation and setting the amount of energy equal to the trap depth U_0, a minimum angle that the scattered particle requires to make for an atom to be lost from the trap, can be found.

$$\theta_{\min} = \cos^{-1}\left(1 - \frac{U_0 m_t}{\mu^2 |\vec{v_r}|^2}\right) \tag{2.66}$$

Recalling that the cross section depends on the scattering amplitude by

$$\frac{d\sigma}{d\Omega} = |f(k, \theta, \phi)|^2 \tag{2.67}$$

the total elastic collision cross section can be re-written as;

$$\sigma = \int_0^{\pi} 2\pi |f(k, \theta)|^2 \sin\theta d\theta \tag{2.68}$$

Using the minimum angle as an indicator on whether or not a particle escapes the trap, allows for the definition of the loss cross section as

$$\sigma_{\text{loss}} = \int_{\theta_{min}}^{\pi} 2\pi |f(k, \theta)|^2 \sin\theta d\theta \tag{2.69}$$

and the heating cross section

$$\sigma_{\text{heating}} = \int_0^{\theta_{min}} 2\pi |f(k, \theta)|^2 \sin\theta d\theta \tag{2.70}$$

Using Eq. 2.69 and modeling the background gas as a Maxwell-Boltzmann distribution we get the $\langle \sigma_{loss} v \rangle$ term to be

$$\langle \sigma_{\text{loss}} v \rangle = \int_{\theta_{min}}^{\pi} 2\pi |f(k,\theta)|^2 \sin\theta d\theta \int_0^{\infty} \sqrt{\frac{m}{2\pi kT}}^3 4\pi v^2 e^{\frac{mv^2}{2kT}} dv \tag{2.71}$$

which which can solved using the scattering amplitude $|f(k,\theta)|^2$ described in the previous section.

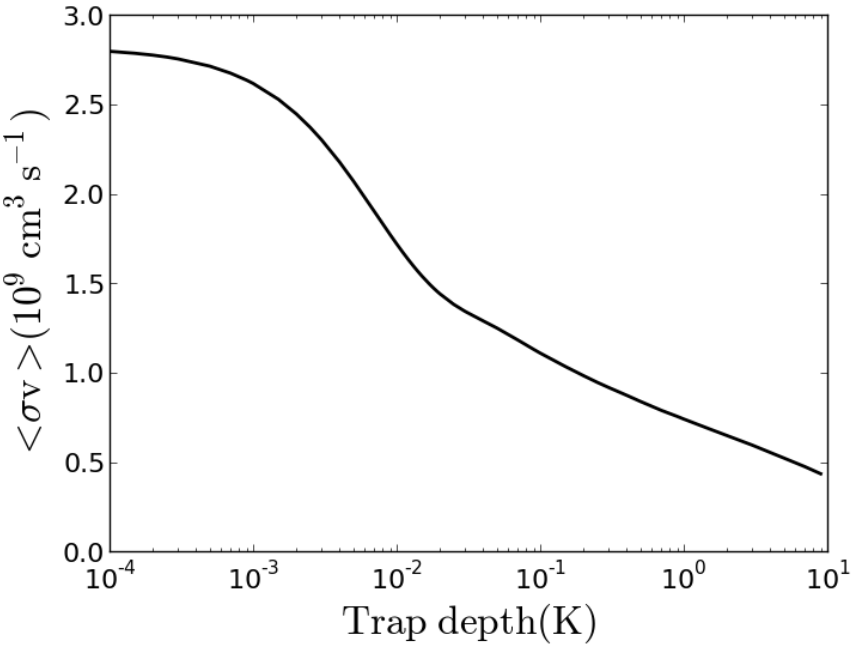

Figure 2.9: Cross section averaged over the velocity of the background gas for Ar and Rb collisions vs. the trap depth. This illustrates how the loss cross section varies with trap depth. The potential used is a Lennard-Jones potential. The C_6 used in this calculation is $280 E_H a_B^6$ and C_{12} is $8.6 \times 10^7 E_H a_B^{12}$, where $E_H = 4.35974 \times 10^{-18}$ J and a_B is the Bohr radius.

Chapter 3

Experimental Apparatus and Procedure

This chapter is comprised of two sections: the experimental apparatus, where the setup and its components are discussed, and the experimental procedure, where the method of creating and preparing the cold atoms as well as implementing the measurement scheme is examined. The experimental apparatus consists of many different sections ranging from the optics that control the light used in creating the sample, to the vacuum required to trap and maintain the sample, and finally to the devices used to measure fluorescence, vacuum pressure, contamination, etc. Moreover the experimental procedure focuses on the preparation of the atoms.

3.1 Experimental Apparatus

The experimental setup is comprised of a vacuum chamber which has three main regions: a 2D MOT, a 3D MOT and the gauge region. The 2D MOT generates a cold beam of atoms from a Rb vapour and is created by two pairs of countering propagating laser beams and a quadrupole magnetic field created by 4 separate race-track coils. The atoms are accelerated out of the 2D MOT region by a "push beam" detuned to the blue of the resonance. The atoms are then trapped in the 3D chamber by a 3D MOT and it is here where the pressure measurement is made. The gauge region includes a Residual Gas Analyzer (RGA), which measures the composition of the background in the setup, as well as two spinning rotor gauges (SRG) and two ionization gauges (IG). One of the IGs and SRGs were provided and calibrated by NIST. Two types of gauges are employed because of their different operational ranges. The SRG (1×10^{-2} to 5×10^{-7} Torr) is used in the high vacuum range and the IG (1×10^{-3} to 2×10^{-11} Torr)is used in the ultra-high vacuum range. The Fig. 3.1 shows the three different regions of the vacuum chamber in detail as well as the port used to introduce gases for the pressure measurement.

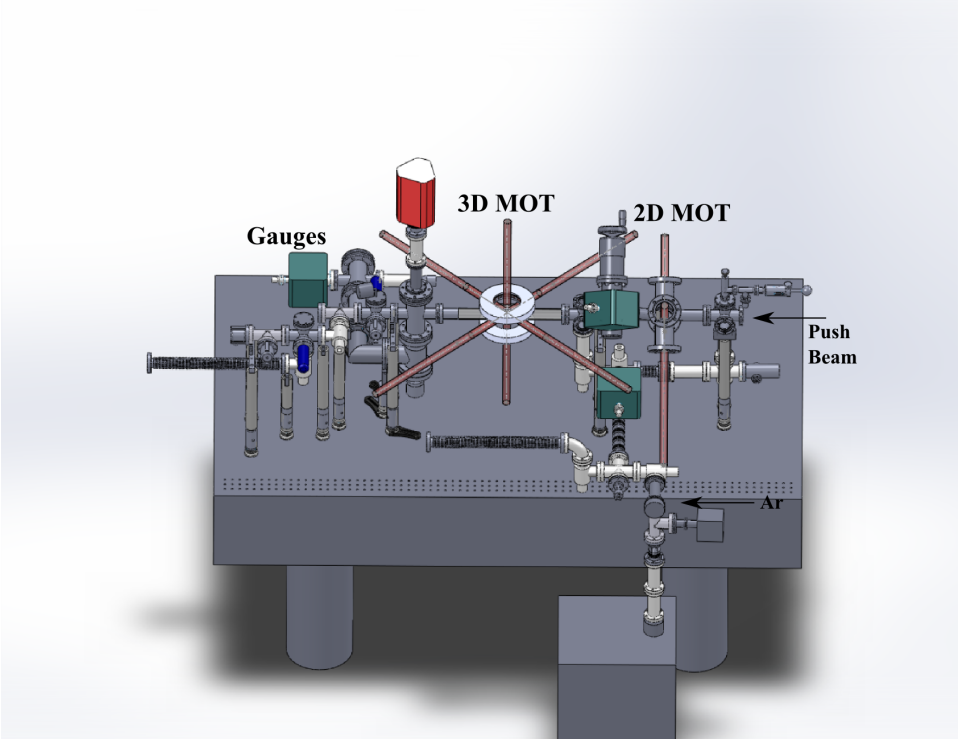

Figure 3.1: The experimental apparatus consists of three main sections; a 2D MOT, a 3D MOT and a Gauge region. A cold flux of atoms is created by a 2D MOT. This cloud is set in motion by a "push" beam to the 3D MOT section. In the 3D MOT section atoms are held in both a MOT and MT. The gauge region next to the 3D MOT is where all the gauges are located[9].

3.1.1 Optical Setup

The optical setup of the experiment is illustrated in the Fig. 3.2. The light is generated on a separate "master" table where it is then sent through fibers to the optical table for the experiment. The light is then amplified by other laser diodes and a tapered amplifier (TA). The polarization and frequency are controlled by additional optics following amplification. After this stage the light is split and sent to the different regions of the apparatus, to supply the light needed to trap the atoms.

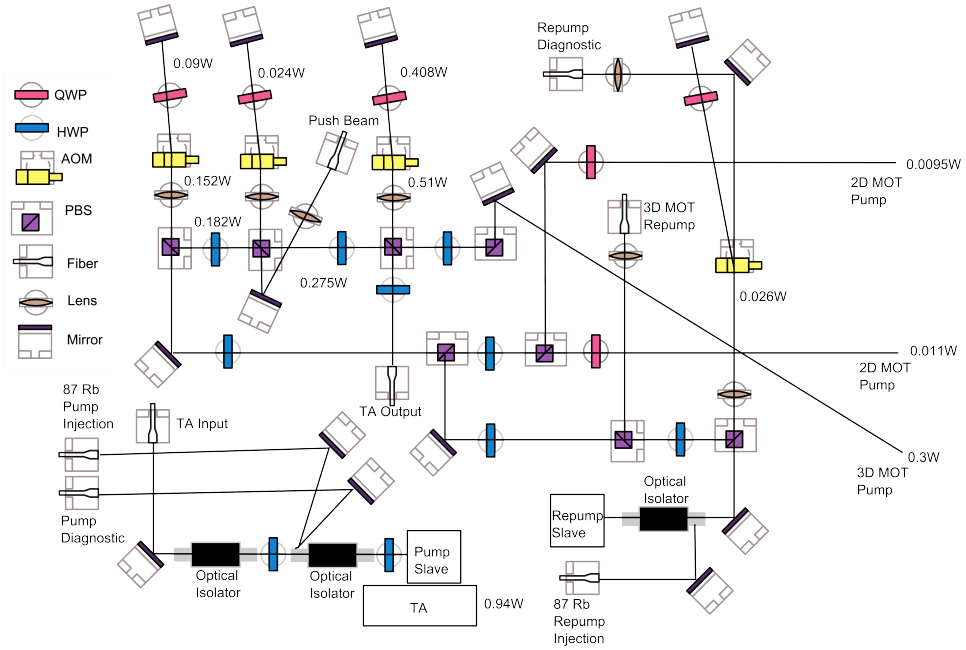

Figure 3.2: Diagram of the optical setup used to generate the laser light for the experiment. We take light from a frequency stabilized master table, amplify it, shift its frequency, and then send the light to the 2D and 3D MOTs[9].

The intensity of the 3D MOT pump light is stabilized using a feedback loop consisting of a PID controller and a photodiode (PD).The light that is sent to the 3D MOT region is sampled by a beam splitter and sent to a photodiode. The reading is compared to a preset voltage to generate the error signal for the PID controller. The controller maintains a constant intensity by feeding back to an r.f. attenuator that regulates the r.f. power sent to the AOM that sets the 3D MOT power. A schematic of the intensity stabilization system is shown in Fig. 3.3.

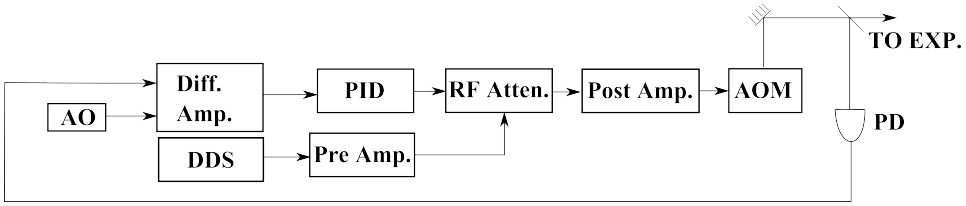

Figure 3.3: Block diagram of the intensity stabilization system of the 3D MOT laser. The setup consists of the following: an Acousto-Optical Modulator (AOM), Photodiode (PD), Analog Output (AO), Differential Amplifier (Diff. Amp.), Pre-amplifier (Pre Amp.),RF Attenuator (RF Atten.), Direct digital synthesizer (DDS). The DDS generates the r.f. signal that is used to drive the AOM.

3.1.2 RF Knife

The RF knife is a key component for setting the trap depth in the magnetic trap. The parts necessary to create the oscillating B-field are shown in Fig. 3.4. The r.f. system begins with a direct digital synthesizer (DDS) that generates the RF signal that is sent to the coil. This signal is amplified with a pre-amplifier and post-amplifier where it is sent through the coil and then attenuated and terminated with a 50Ω load. The attenuator and terminating load are used to minimize reflections back into the post amplifier.

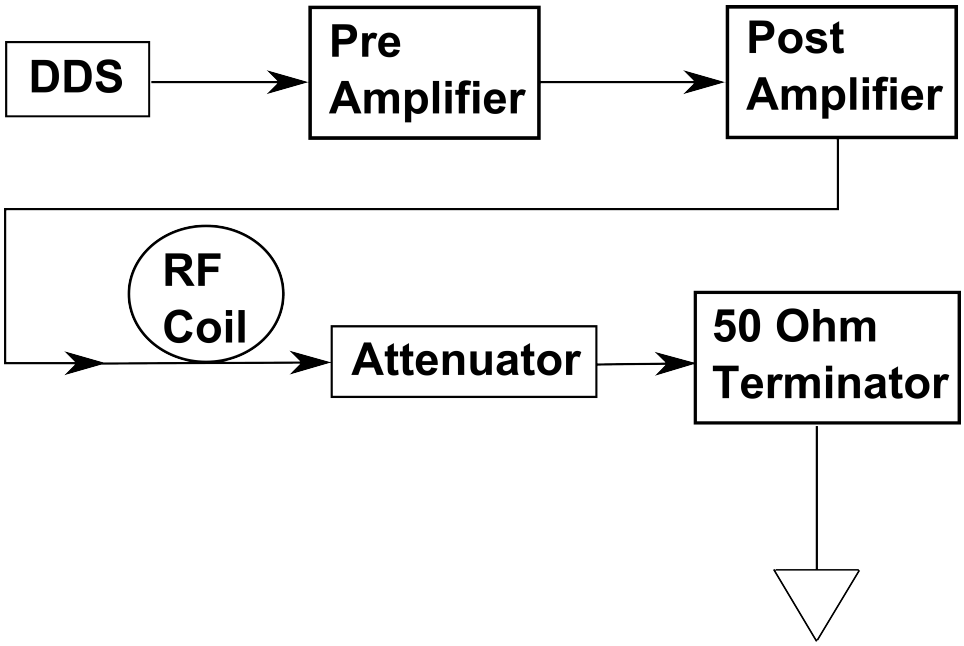

Figure 3.4: Block diagram of of the RF knife used to set the trap depth of the atoms in the magnetic trap.

The RF coil is created by taking a RG-174 coax cable and stripping its outer sheath to expose the inner conductor. The sheath is reconnected at the loop beginning and end. A single loop is used to maximize the bandwidth of the antenna, given that a large frequency range (500kHz-140MHz) is desired.

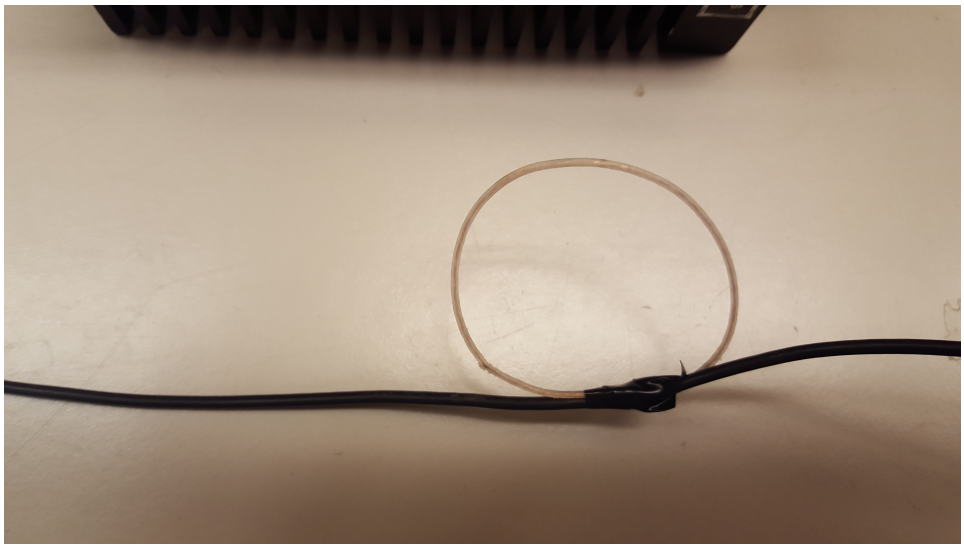

Figure 3.5: Picture of the RF coil used in the experiment. It is a single looped stripped BNC whose outer sheath is removed and the ends of the sheath are soldered together to continue the cable intact to the termination resistance.

The transmission characteristic of the RF coil can be seen in the figure below. Here one end of the coil was connected to a network analyzer (HP8753E) and other end terminated with 50Ω. The reflectance as a function of the frequency was measured. From the Fig. 3.6 there is a clear roll off of reflectance for lower frequencies, where the coil acts as a short.

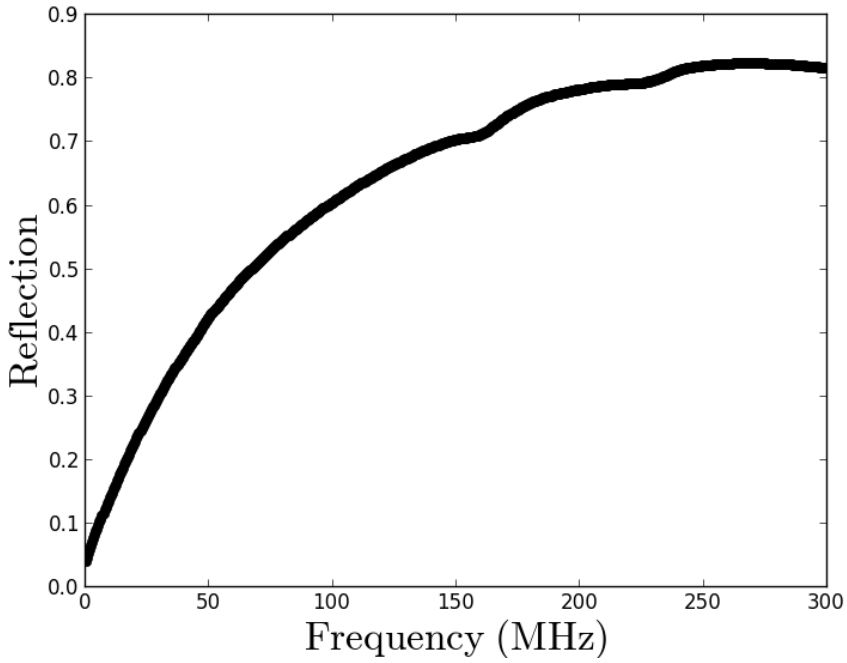

Figure 3.6: This is a plot of the reflection characteristic of the RF coil. The measurement was made by connecting the the RF coil to a network analyzer (HP8753E) and recording the reflection as a function of frequency. One can see a drop off of the reflected (hence increase in transmitted) power in the lower frequencies, where the coil acts as a short. On the high end, the loop reflects a majority of the power acting as a high impedance.

3.2 Experimental Procedure

The experimental procedure involves the method for producing, controlling the cold atoms and executing the experiment. The procedure has a few key steps that are necessary to prepare the atoms and to ensure the reproducibility of each measurement. Also each step is optimized to maximize the number of atoms in the trap and the signal to noise ratio.

3.2.1 Overview

The atoms are first collected from a vapour and loaded into a 2D trap where the are sent to the 3D trap. From here they are further cooled, optically pumped into the correct quantum state and captured in the magnetic trap. Then, the most energetic atoms are ejected from the MT and the remaining atoms are left to interact with the background gas. As measurements are made of the remaining atoms in the trap for various holdtimes, a loss rate can be extracted. This loss rate is then used to determine the background density of gas.

The timing diagram is shown in Fig. 3.7 and indicates the optimal timings found for each stage that minimize heating and atom loss in the preparation steps.

Figure 3.7: Timing diagram of the experiment showing the optimal timings found for each stage that minimize heating and atom loss in the preparation steps.

3.2.2 The 2D MOT

The atoms are loaded into the 3D MOT from the 2D trap. The 2D MOT consists of a pair of crossed beam. Each beam passes through a pair of coils which generates the magnetic field for the 2D MOT. The atoms are cooled and trapped from a room temperature gas. The atoms that enter the center of the 2D MOT region are accelerated in the direction of the 3D MOT by a separate push beam. The loading rate from the 2D limits how high in pressure a loss rate measurement can be performed, because the steady state atom number is dependent on the ratio of the loading rate and loss rate. During this loading the fluorescence of the 3D MOT is monitored and a typical loading signal is shown in Fig. 3.8.

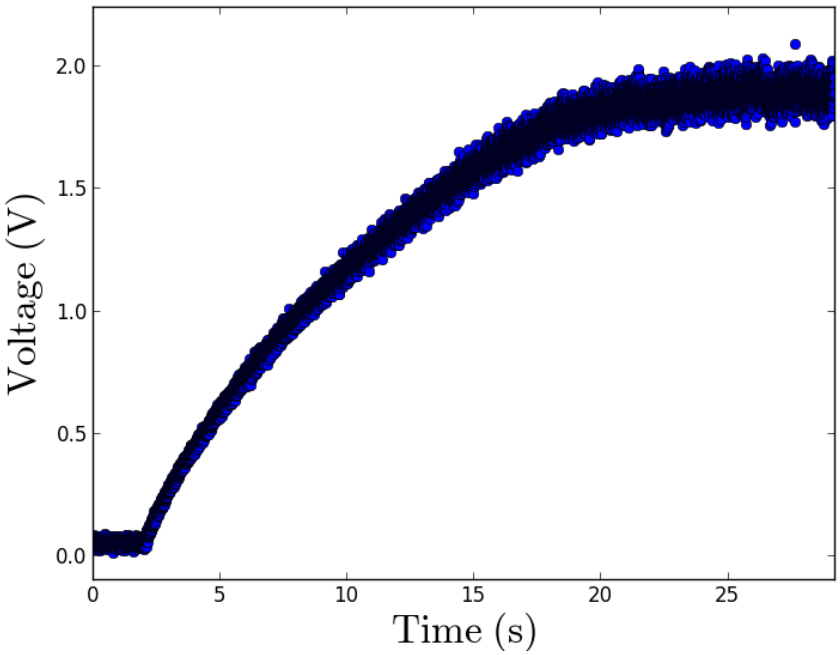

Figure 3.8: Fluorescence vs. time of a 3D MOT. The curve can be model by the loading Eq. 2.8 or Eq. 2.11 depending on which regime the MOT fills to. Here the MOT turns on after an initial 2 second wait period.

3.2.3 Sensor Ensemble Preparation in the 3D MOT and Transfer to the MT

When atoms are loaded into the 3D MOT, measures are taken to ensure the constant density regime is reached in the MOT since this produces the lowest shot-to-shot variation of atom number. The atoms are cooled and optically pump to the lower ground state ($F = 1$), the optimization of these stages are discussed in section 3.2.5. Atoms are loaded for different amounts of time and transfered into the MT and then recaptured again in the 3D MOT to determine the number transfered. The number in the MT saturates above a certain number in the 3D MOT and therefore the MOT is always loaded to an atom number beyond this point to minimize number fluctuations. Fig. 3.9 shows that, initially, as the MOT atom number increases so does the recaptured amount. However once 6×10^8 atoms in the MOT is reached, the recaptured number levels off. Fig. 3.9 also shows that the maximum number loaded into the MT and the saturation point depends on the depth of the MT as set by the RF knife. For a fixed magnetic field gradient, more atoms are captured by the MT for a larger trap depth because the spatial volume is larger for a deeper trap.

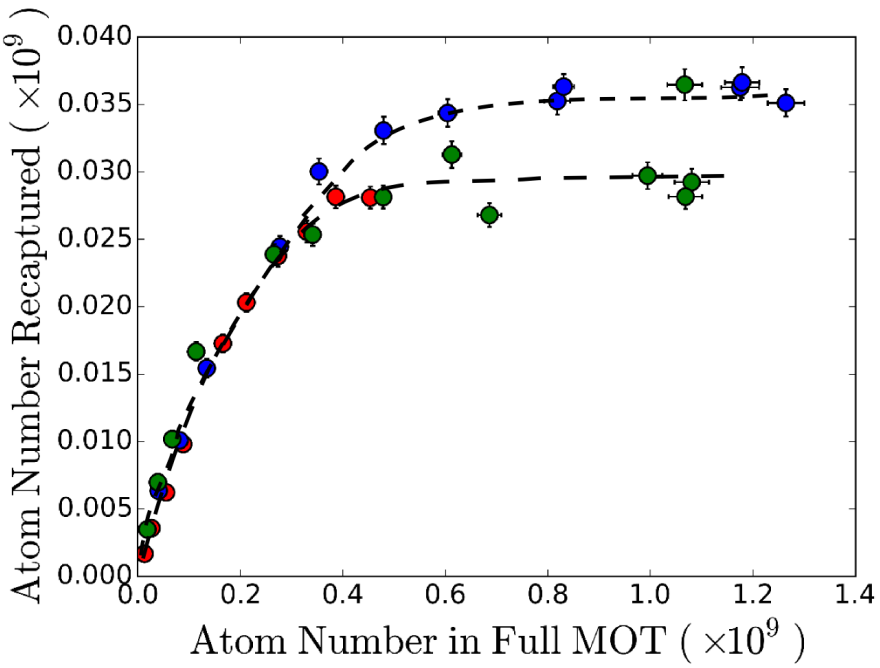

Figure 3.9: Atom number loaded into and recaptured from the MT as a function of the initial number in the 3D MOT for different MT depths set by the RF knife. This figure illustrates when the constant density regime has been reach. The GREEN and RED plots correspond to a 5MHz trap depth and the BLUE corresponds to 10MHz. It can be seen that after 6×10^8 atoms the MOT enters a constant density regime because the number of atoms recaptured is becoming insensitive to the total atom number. Also the steady state value for the 5MHz and 10MHz trap depths differ because the 10MHz trap is spatially larger.

3.2.4 Atom Number Measurement

The measurements of sensor particle loss rate depends on measuring the atom number left in the MT over time, and it is critical that our measurement signal is strictly proportional to the atom number as any non linearity will result in a systematic error in the loss rate. Fluorescence measurements of the recaptured atoms in the 3D MOT are the most convenient; however, we need to calibrate the fluorescence signal to the atom number and verify

that the signal is linear in the atom number. Therefore an optical pumping technique is employed as an independent method to count atom number. The technique involves taking an absorption trace with and without an atom cloud in the path of a probe beam[4]. Fig. 3.10 shows the traces of the probe beam with (RED) and without (BLACK), the difference of the two is shown in Fig. 3.11. Fig. 3.11 represents the amount of photons scattered out of the path of the probe beam. Since the probe beam is set to the $5^2S_{1/2}$ to $5^2P_{3/2}$ transition and each atom scatters a finite number of photons N_γ before falling into the dark $F = 1$ ground state, the atom number is simply $N_{atoms} = \frac{S}{N_\gamma}$ where S is the total number of photons scatter out of the probe beam[4][**?**].

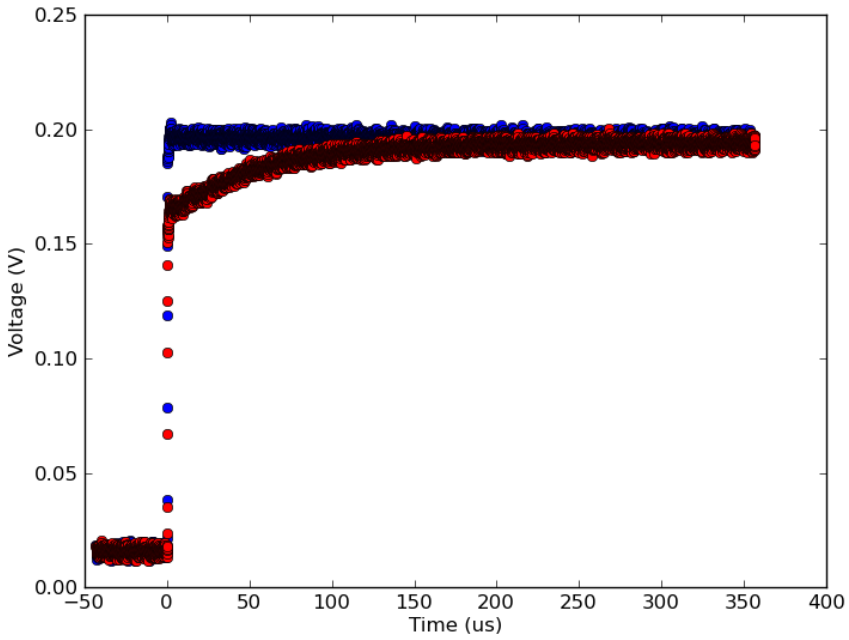

Figure 3.10: Plot of the transmitted intensity of the probe beam used to measure the atom number. The red trace corresponds to a signal with atoms present in the beam path and the black corresponds to one without. The round edge of the red signal is a result of atoms scattering the probe beam, thus reducing the transmitted light. The slight discrepancies in the steady state signal is a result of the background level changing from shot to shot.

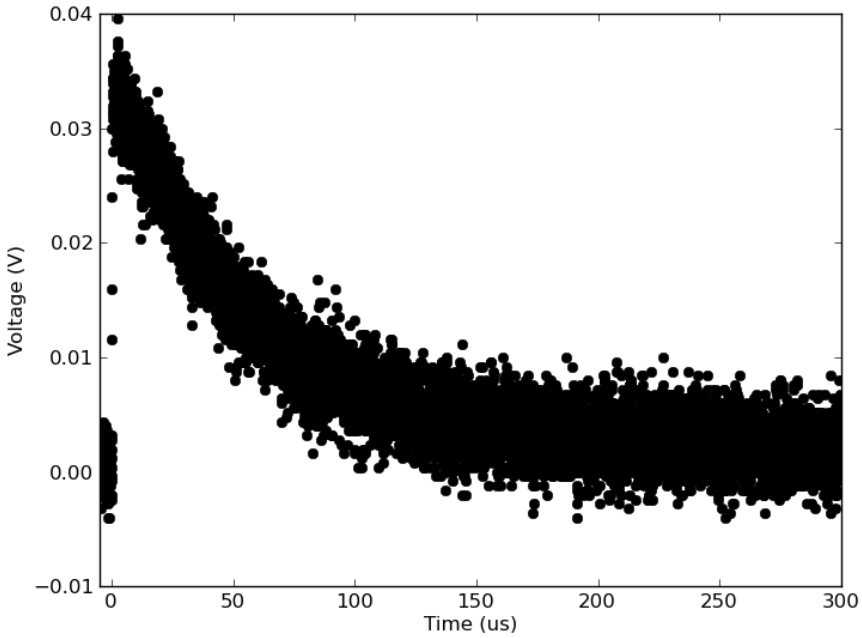

Figure 3.11: Plot of the difference of the probe beam transmitted intensity with and without atoms in its path. We can see that over time atoms are being pumped out of the bright $F = 2$ state by the probe light allowing for more light to transmit resulting in a decrease in the absorption signal. The area under the curve is related to the total number of atoms in the path.

By measuring the atom number and fluorescence for different amounts of atoms a calibration curve between atom number and fluorescence can be obtained. This curve shown in Fig. 3.12 allows for the determination of atom number solely from fluorescence. The advantage of a fluorescence measurement versus an optical pumping measurement is that the signal to noise for a fluorescence measurement is much higher than optical pumping. It is for this reason that all measurements are made using fluorescence.

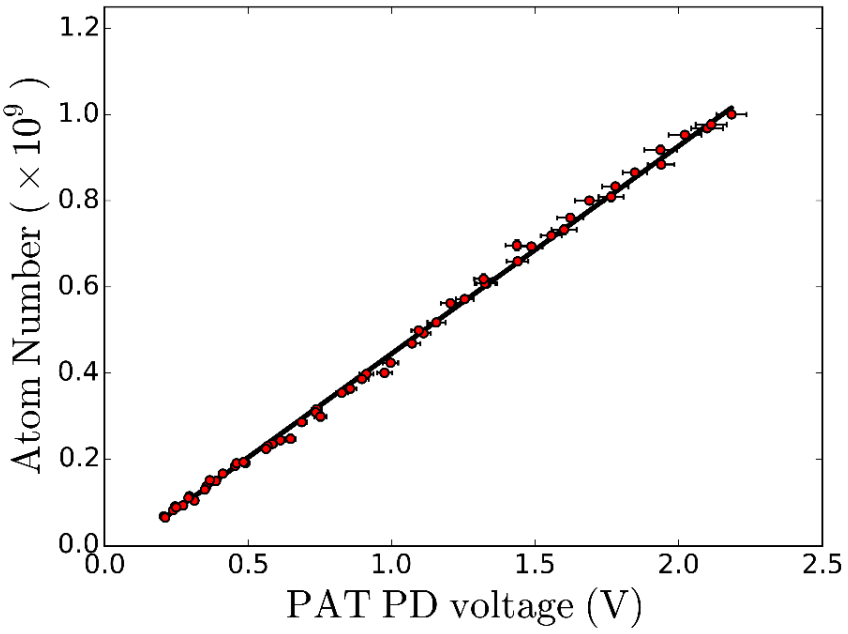

Figure 3.12: Atom number as measured by optical pumping induced by a probe beam versus fluorescence of the same atoms in a MOT. We can see a linear relationship between them for atom numbers in the range from 1×10^9 to 5×10^7 atoms. This provides a calibration for fluorescence signal to atom number. The calibration factor is approximately 5×10^8 per volt.

3.2.5 Optimization

There are many parameters to optimize in the experiment. In particular hyperfine pumping and cooling stages are looked at to maximize the number and minimize temperature of the atoms loaded into the MT and to ensure state purity. Cooling of the atoms before transfer in MT is accomplished by detuning the light away from resonance and holding the atoms in that light for a period of time. The optimization was carried out at several different frequencies for various holdtimes. The results are summarized in Fig. 3.13. It appears that holding the atoms for 75 ms at a 60 MHz detuning maximizes the number of atom recaptured in a MT trap depth of 180μK. These values are used in the experiment.

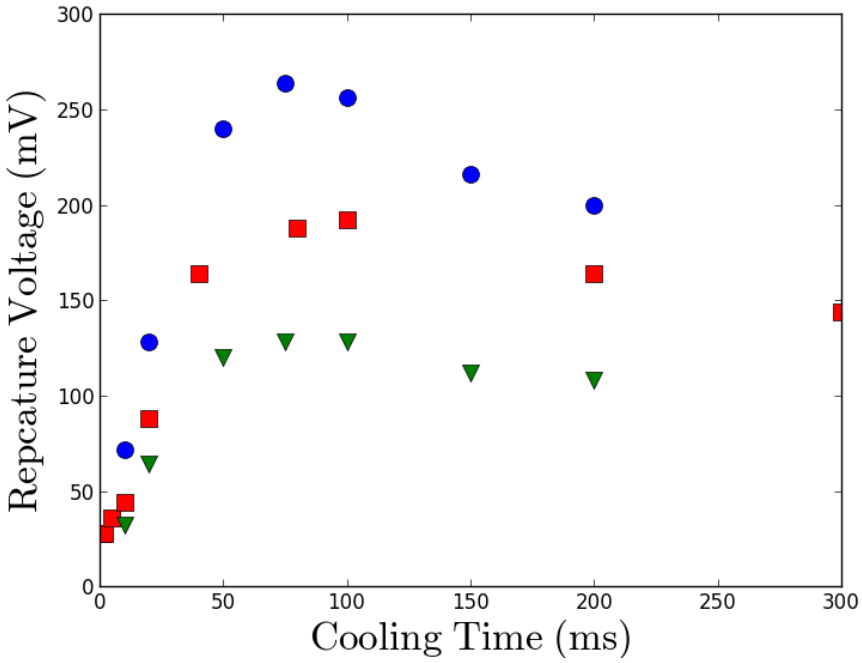

Figure 3.13: Atom number loaded into and recaptured from the MT as a function of cooling duration for various detunings: 60 MHz(blue circles) 50 MHz(red squares)and 40 MHz (green triangles). One can see a maximum occurring at a duration of 75 ms for a detuning of 60 MHz.

To ensure that atoms that are transfered into the MT are in the lower hyperfine state, the repump is turned off for a period of time before the pump light is extinguished allowing the atoms to pump to the $F = 1$ ground state. The amount of atoms captured in MT is measured and the results are shown in Fig. 3.14. From the results 2 ms was chosen as the optimal value for the experiment.

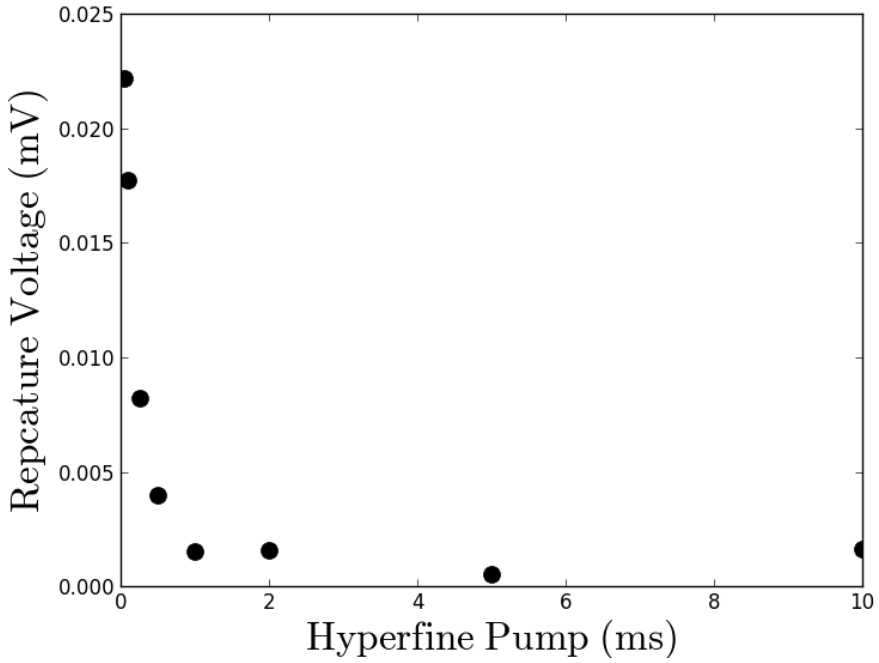

Figure 3.14: Atom number in the $m_F = 2$ state loaded into and recaptured from the MT as a function of the hyperfine pumping time. Spin filtering (discussed in section 2.2.2) was used to remove any atoms in the $m_F = 1$ state and detect only those atoms in the $m_F = 2$ state. Since atoms in the $m_F = 2$ state can only be in the upper hyperfine state ($F = 2$), this signal provides a measure of the hyperfine pumping efficiency.

3.2.6 Ensemble Preparation

The atom number in the MT is not the only parameter which needs to be optimized. In particular, the energy distribution plays a key role in determining if the cloud is suitable for the measurement. In short the atom temperature should be small compared to the depth of the MT for a loss measurement. The atoms in the MT can be modeled by a Maxwell-Boltzmann distribution with an offset in the energy. This offset is the minimum energy for the ensemble set by Majorana losses and any mis-match between the MOT and MT centers. Here Fig. 3.15 shows a typical potential energy distribution for the experiment. Here the average temperature is 161μK and the offset is

1.45MHz or (72.5μK). This temperature is cold enough to have a suitable amount in a shallow magnetic trap.

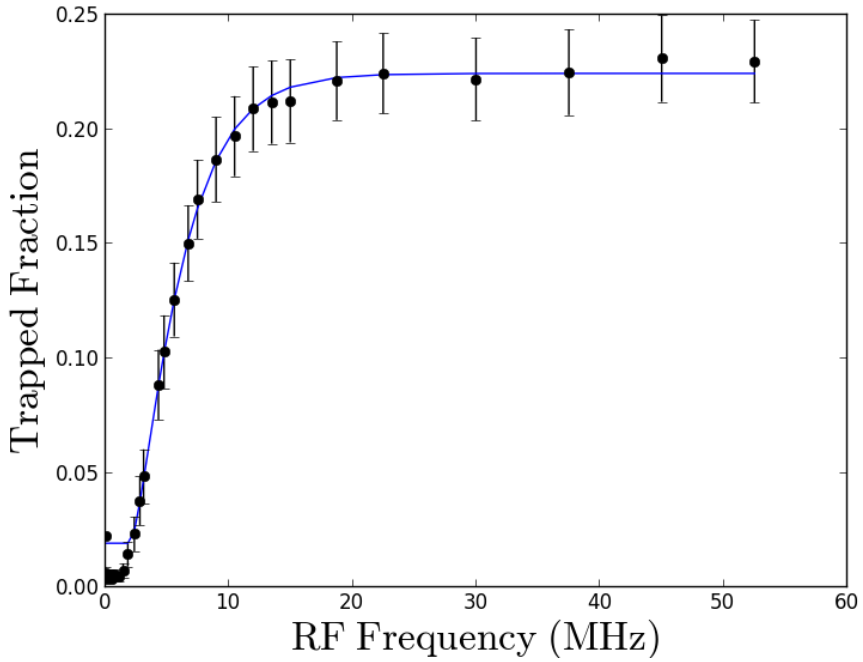

Figure 3.15: Trapped fraction in the MT versus the lower frequency in a radio frequency sweep used to remove atoms with energy above the cutoff $E_c = hf_{lower}$. From the profile one can extract the temperature (energy distribution) and the energy offset of the atoms in the magnetic trap. This profile corresponds to a temperature of 161μK and an offset of 1.45 MHz(72.5μK).

To verify the efficiency of the RF knife in clearing out atoms above a certain energy level, the amount of time it takes to empty the trap was examined. The time it takes for the trap to be emptied at various powers is shown in Fig. 3.16. It shows that at 30 W it takes about 0.7s seconds to empty out the trap, this sets the minimum time that the measurement can take place.

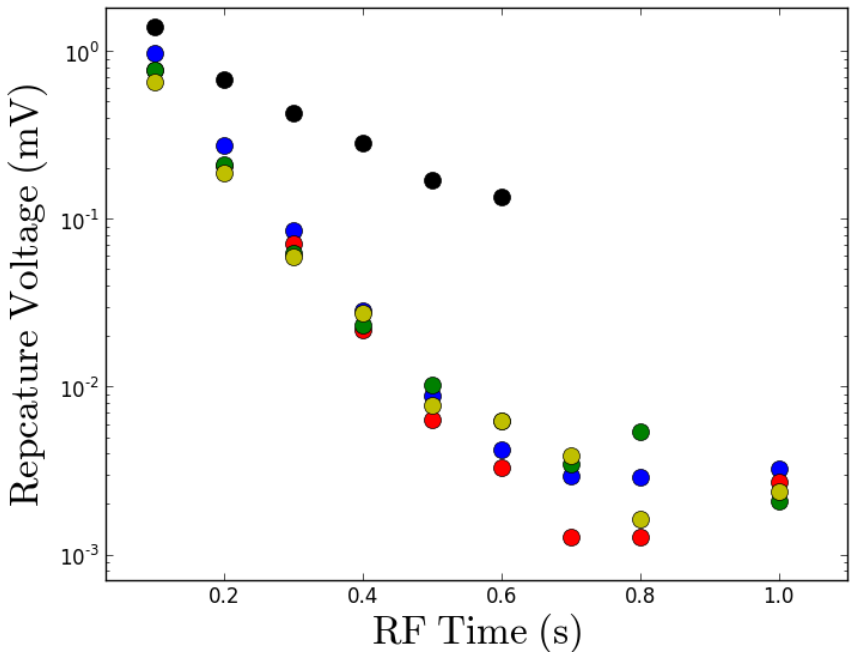

Figure 3.16: Recaptured atom signal from the MT versus the RF exposure time for various RF powers. The RF consists of a "triangle frequency ramp" from 140 MHz to 1 MHz at rate of 100 GHz/s used to empty atoms from trap. The various powers correspond to RF powers of 0.74 W(Black), 4.65 W(Blue), 8.26 W(Red), 12.5 W(Green) and 30 W(Yellow). Here one can see that the recapture voltage decreases until it levels off after roughly 0.6 seconds providing an empirical measure of the minimum RF time required to eject atoms from the trap and thus to set the maximum ensemble energy level in the trap.

Chapter 4

Pressure Measurement Results

This chapter reports on measurements of the decay of trap population over time (here after called a decay trace) with and without argon added to the vacuum chamber. The measurements without Ar are needed to determine the baseline and to assess the performance of the system. Following this, argon was added to the system and loss rates were measured. The measurement technique is as follows:for each pressure being studied a decay trace at three different trap depths in the MT is recorded as well as a MOT decay trace. From each trace a loss rate is extracted and a pressure is inferred from the $\langle \sigma v \rangle$ calculation. This pressure is compared to the pressure measured using an ionization gauge (IG) allowing us to extract the IG calibration factor for that gauge for the gas being introduced (argon).

4.1 Loss Rate Measurement

Figure 4.1 illustrates how the measurement is executed. Fig. 4.1 shows the complete experimental run, while Fig. 4.2 shows a zoomed in view which can be examined more carefully. As seen in the figure, atoms are loaded into the 3D MOT and held with the 2D MOT off so there is no longer any loading. The trapped atoms are then cooled and optically pumped in the lower hyperfine state $F = 1$. From here they are transferred to the magnetic trap where they are held for another period of time and exposed to an RF signal setting the trap depth. Next the atoms are re-captured in the 3D MOT and re-imaged to see how many are left in the trap, after which the trap is emptied by turning the magnetic field off. Finally a background signal produced by scattered light is measured and the experiment is repeated.

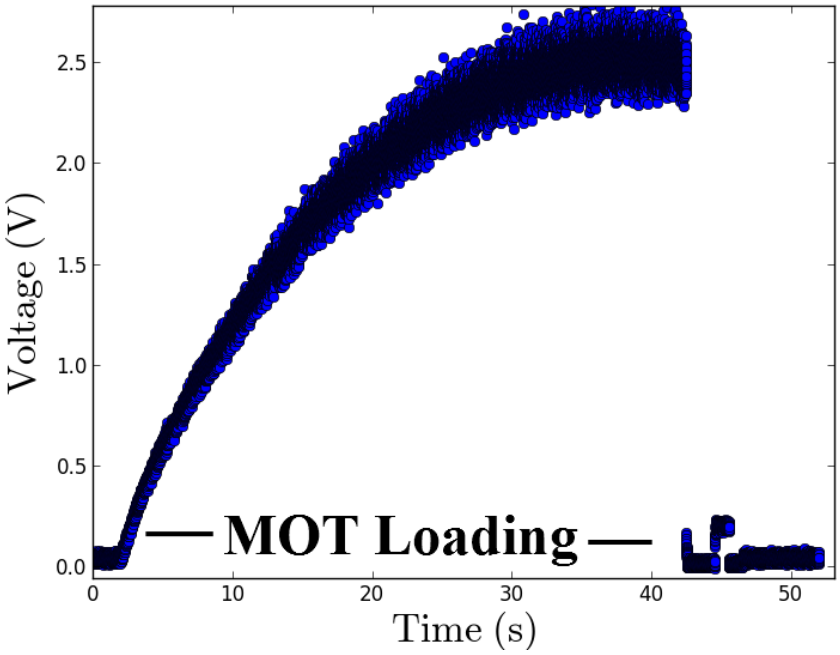

Figure 4.1: MOT fluorescence versus time for a single magnetic trap lifetime measurement. Atoms are loaded in to the 3D MOT then transfered to the MT and held for some time during which losses occur, recaptured in the MOT, re-imaged, then emptied out.

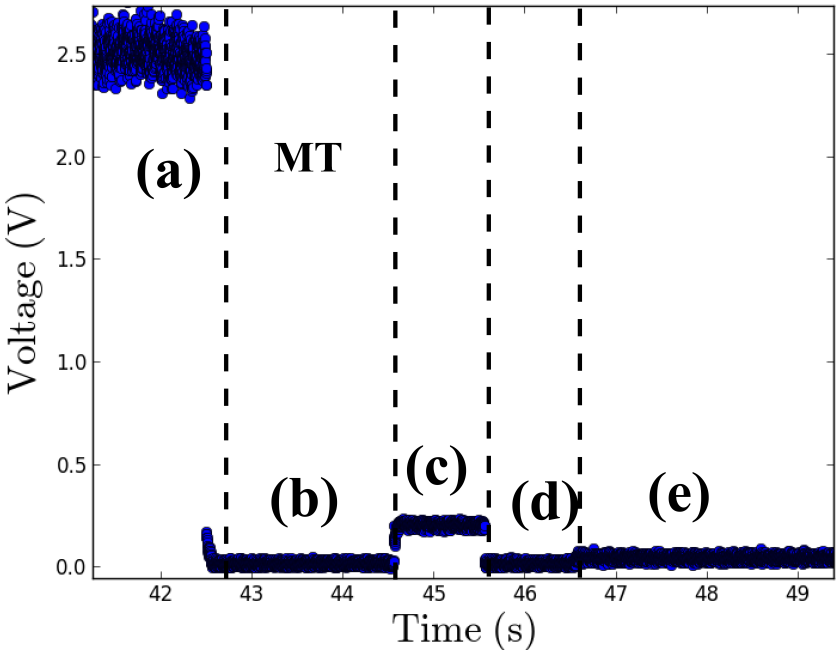

Figure 4.2: Shows a zoomed in view of the experimental run. In stage (a), the 2D MOT is turned off and a drop in 3D fluorescence is seen. In stage (b) the atoms are cooled and optically pumped for about 100 ms and transfered to the MT. In the MT, the light is off and the atoms are held for various amounts of time. In stage (c), the atoms remaining in the MT are recaptured in the 3D MOT re-imaged by the trapping light. In stage (d), the MOT is emptied. In stage (e) the MOT light is turned on but with the MOT magnetic field off to obtain a scattered light background reading. The fraction recaptured is determined by the ratio of the voltage in stage c to stage a.

Fig. 4.3 shows the recaptured atoms from the MT as a function of the holdtime in the MT. The fraction is given by

$$f = \frac{V_c - V_e}{V_a - V_e} \tag{4.1}$$

The trap population is given by Eq. 2.6 In the dilute limit (i.e. when intra-

trap loss is negligible) Eq. 2.6 reduces to a simple differential equation

$$\dot{N} = -\Gamma N \tag{4.2}$$

whose solution is

$$N = N_0 e^{-\Gamma t} \tag{4.3}$$

The data is fitted to this exponential decay function and Γ is extracted.

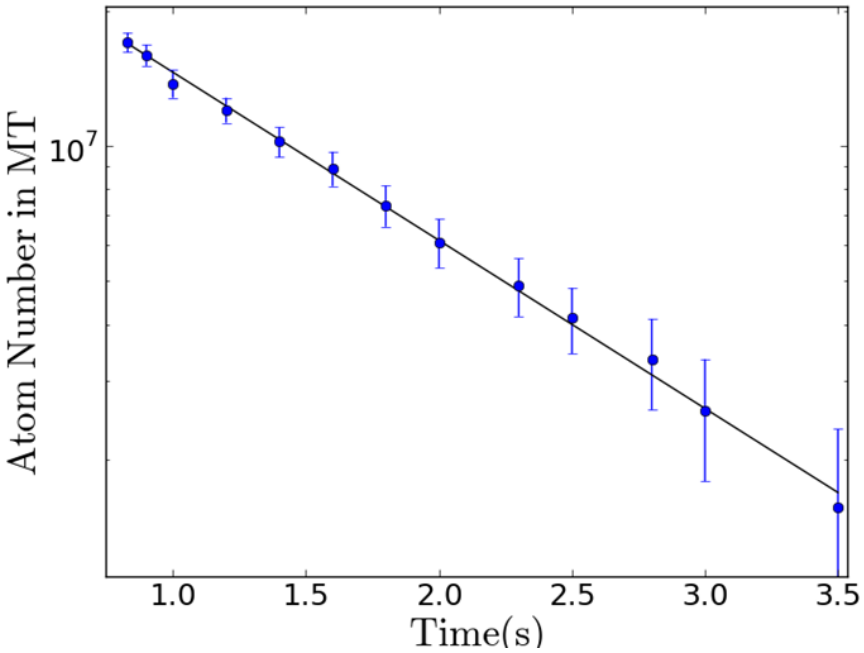

Figure 4.3: Semilog plot of the number of atoms remaining in the magnetic trap as a function of time. An exponential decrease in the atom number as a function of time is observed. The lifetime is 2.5s and the background pressure at which the trace was taken is 5.0×10^{-9} Torr. The background is mostly H_2 in this case.

A loss rate can also be determined by measuring the decay of the 3D MOT population when the loading from the 2D MOT is turned off. Fig. 4.4 shows the decay of fluorescence from the atoms in the 3D MOT. For large MOTs, the dilute approximation can usually not be applied. Therefore, a

more general approach is taken to model the decay, described in Eq. 2.6.

$$\dot{N} = -\Gamma N - \beta \int n^2(\vec{r}, t) d^3\vec{r} \tag{4.4}$$

If, as the MOT grows in number, it grows in volume at a constant density the the above expression can be rewritten in the constant density regime as

$$\dot{N} = -\Gamma N - \beta \overline{n} N \tag{4.5}$$

where

$$\overline{n} = \frac{1}{N} \int n^2(\vec{r}, t) d^3\vec{r} \tag{4.6}$$

and the solution as

$$N = N_0 e^{-\Gamma_{\text{eff}} t} \tag{4.7}$$

Here, the effective loss rate is $\Gamma_{\text{eff}} = \Gamma + \beta\overline{n}$. For sufficiently small MOT numbers, the density is low enough and the loss is dominated by background collisions. Here the intra-trap two body loss contribution to the decay is negligible reducing Eq. 4.7 back to the dilute limit. However the loss rate in the MOT is not the same as the loss rate in the MT even in the dilute limit since the cross section for loss is different. In the MOT, atoms are both in the ground state and excited state, and each state has its own unique loss cross section. This difference in cross section occurs because the intra-molecular potential for the background gas particle with the Rb atom in the excited state and the ground state differ. In the case of an excited state Rb atom colliding with an Ar atom, the potential energy surface is anisotropic and the collision cross section depends on the orientation of the Rb atom.

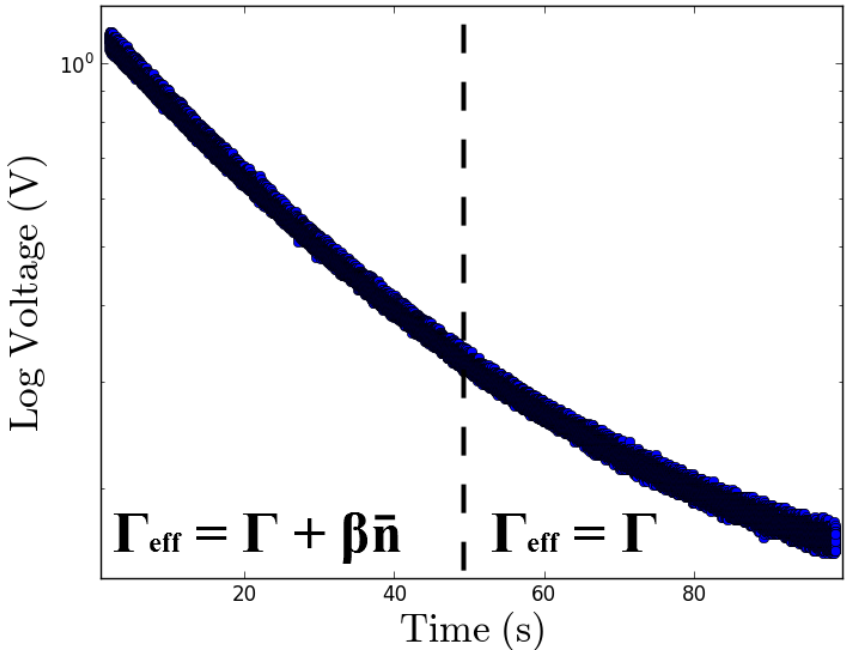

Figure 4.4: Decay of the 3D MOT fluorescence as a function of time. From this one can extract the loss rate due to intra-MOT collisions and due collisions with the background vapour, by looking at the different regions of the curve. The first region (before 50s) is dominated by both loss due to intra-MOT collisions and background gas collisions the second region(after 50s) is predominately due to background gas collisions.

To determine if the MOT is or is not in the dilute limit, a trace of the decay is taken as in Fig. 4.4. The figure is examined carefully to establish if the decay can be modelled by a single exponential decay. The tail end of the data (50s and longer) is fit to extract the loss rate mainly due to the background collisions.

4.2 Argon Measurement

The argon pressure measurement requires a knowledge of the loss cross section of an argon and rubidium collision which is summarized in Fig. 4.5, showing the loss rate coefficient, $\langle \sigma v \rangle$ for multiple trap depths. For deep

traps ($> 1K$) the loss rate coefficient decreases with increasing trap depth but as the trap depth becomes shallower the loss rate coefficient eventually levels off approaching the total loss rate.

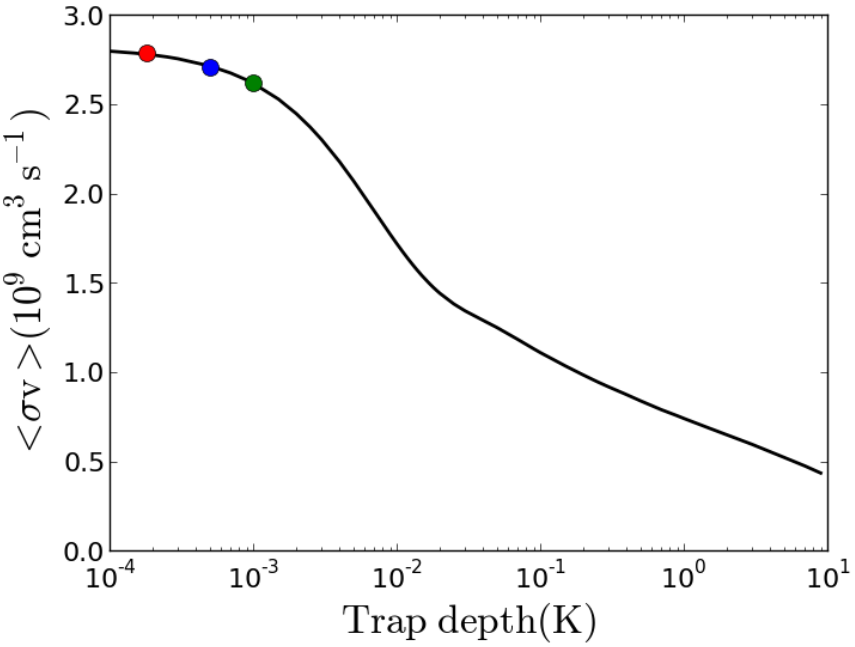

Figure 4.5: Loss cross section averaged over the velocity of the background gas vs. the trap depth. This illustrates how the loss cross section varies with trap depth. The three trap depths used are indicated by the filled circles: 180μK (RED) 500μK (BLUE) 1mK (GREEN).

To extract a pressure from the loss rate measurement the formula below are used.

$$\Gamma = \Gamma_0 + \Gamma_{\mathrm{Ar}} \tag{4.8}$$

$$\Gamma = \Gamma_0 + n_{\mathrm{Ar}} \langle \sigma v \rangle_{\mathrm{U}} \tag{4.9}$$

$$P = n k_{\mathrm{B}} T \tag{4.10}$$

$$P = \frac{\Gamma - \Gamma_0}{\langle \sigma v \rangle} k_{\mathrm{B}} T \tag{4.11}$$

Here Γ_0 is the background loss rate with no argon to the test chamber, k_B is Boltzmann's constant and T is the temperature of the background gas. Fig. 4.6 shows the loss rate as function of the added argon gas for three different trap depths. The three different slopes correspond to the different $\langle \sigma v \rangle$ values. The trap depth mentioned below is the average trap depth that the atoms experience in the magnetic trap, due to the anisotropic nature of the MT.

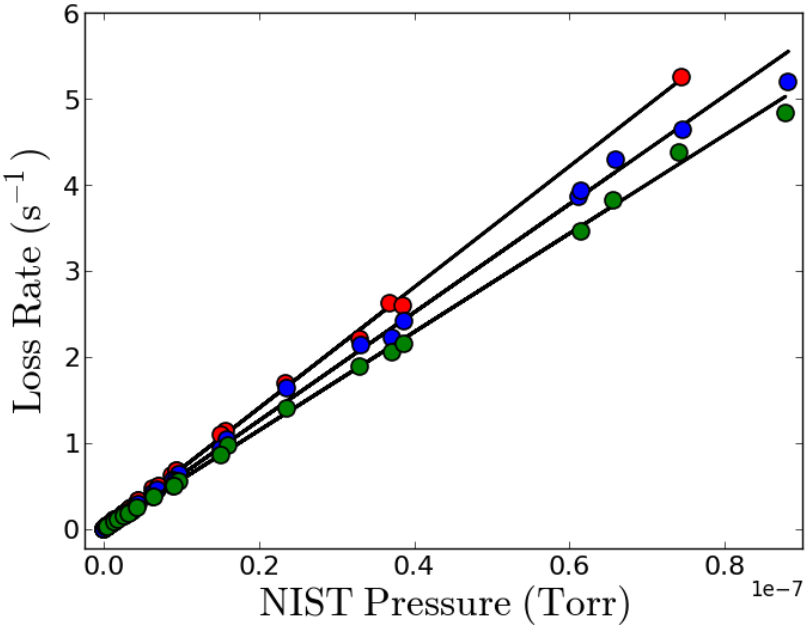

Figure 4.6: Plot of the loss rate as function of the NIST ion gauge reading as Ar was leaked into the system for three different trap depths resulting in different slopes. Each color corresponds to a different trap depth, 0.52 mK (RED) 1.29 mK(BLUE) 2.88 mK(GREEN). Here the trap depth is set by the magnetic field gradient and the laser recapture volume. No RF knife was used.

By applying Eq. 4.11 to the data in Fig. 4.6, Fig. 4.7 is generated. This plot shows a comparison of the pressures measured by the cold atom loss rate and by a NIST calibrated ionization gauge.From the plot the gauge factor can be extracted. The gauge factor is the correction factor needed to

convert the gauge reading to the actual pressure when gases species other than N_2 are measured (i.e. the correction factor for N_2 is 1) The results are summarized in the Table 4.1 below :

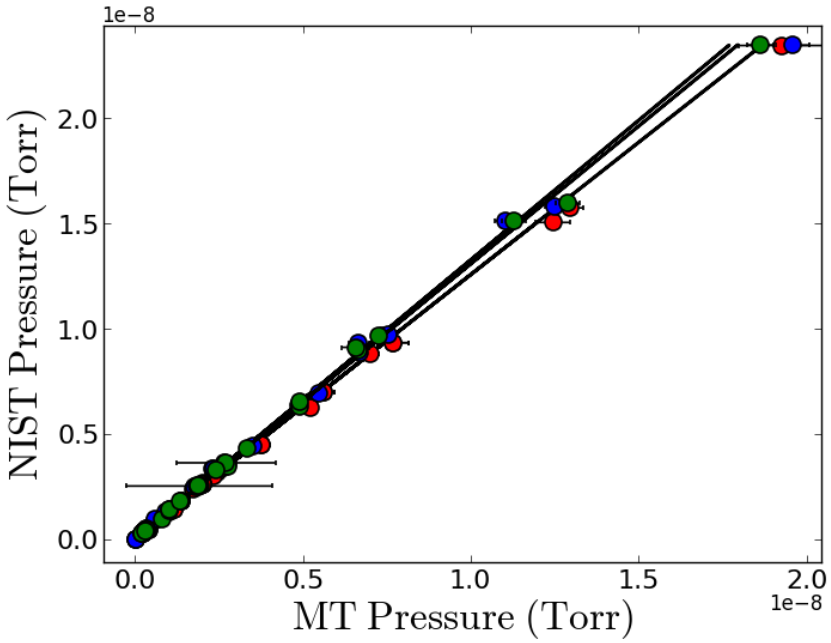

Figure 4.7: Plot of the pressure measured by the cold atoms vs an ionization gauge. The different lines correspond to the data of different trap depths shown in Fig. 4.6, and all collapse into a single curve because the $\langle \sigma v \rangle$ term has been divided out . This line now represents the gas calibration factor of the ionization gauge for Ar, and shows that it is independent of the measurement trap depth.

Trap depth (mK)	Gauge Factor
0.52	1.22(5)
1.29	1.33(3)
2.88	1.30(3)

Table 4.1: Table of gas calibration factors.

From the data in Table 4.1 the average gauge correction factor over all trap depths is 1.29(1), which is in agreement with literature values of 1.3[24]. One simple way of improving the measurement is by using an RF knife to set the trap depth. By using the RF knife, the precision of setting the trap depth is improved and allows for the setting of trap depth to low values where the $\langle \sigma v \rangle$ term becomes less sensitive to depth. Here we remind the reader that the trap depth is not isotropic due to gravitational sag and significantly fewer atoms are transferred to the MT, limiting the SNR. Fig. 4.8 shows the data taken with the depth set by an RF knife.

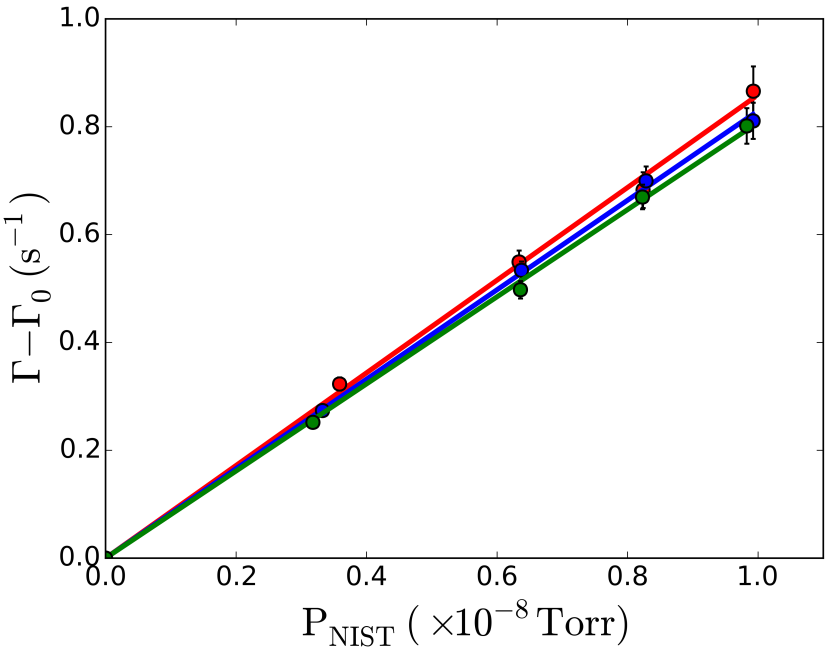

Figure 4.8: Trap loss rate versus NIST ion gauge reading. Here the trap depth for the different traces is set using the RF knife. The trap depths here are 0.18 mK(RED) 0.5 mK(BLUE) 1.0 mK(GREEN).

In using the RF signal to set the trap depth, a slightly different set of trap depths are used. This is because shallower traps are possible and allow for loss measurements in the regime where $\langle \sigma v \rangle$ is closer to the loss rate for a free particle subjected to the argon flux.

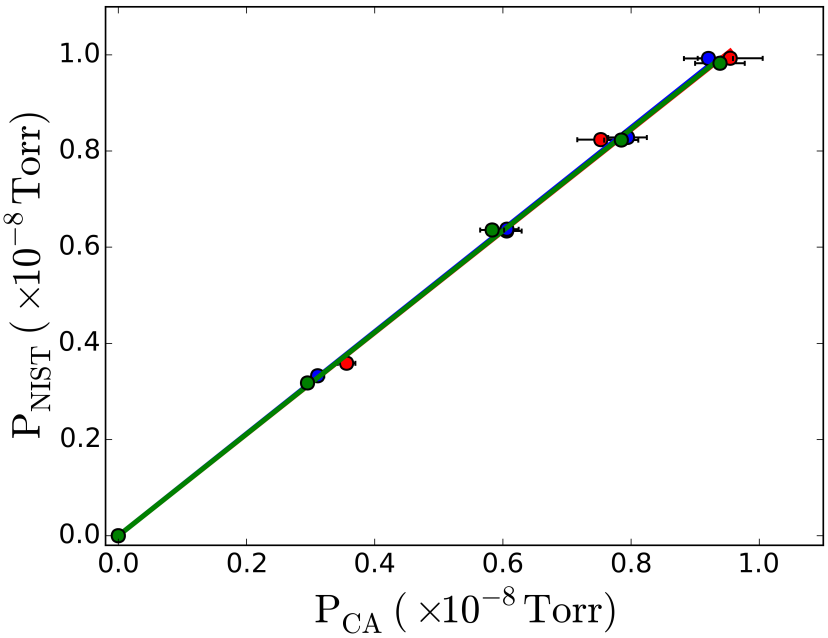

Figure 4.9: Plot of the pressure measured by the cold atoms vs an ionization gauge. The different lines correspond to the data of different trap depths shown in Fig. 4.8, and they all collapse into a single curve because the $\langle \sigma v \rangle$ term has been divided out. This line now represents the gas calibration factor of the ionization gas for Ar, and shows that it is independent of the measurement trap depth.

The table below shows the gas calibration factors determined from the data in Fig. 4.9 for each trap depth when the RF knife is used.

Trap depth (mK)	Gauge Factor
0.18	1.047(34)
0.5	1.073(28)
1.00	1.078(26)

Table 4.2: Table of gas calibration factors with N_2 contamination.

Clearly there is a large difference in the gauge factor reported here com-

pared to those found before in Table 4.1 for the two trials. We discovered that this difference can be attributed to a gas contamination introduced by a faulty leak valve. This was discovered when an RGA was used to check all contaminants. The results are below;

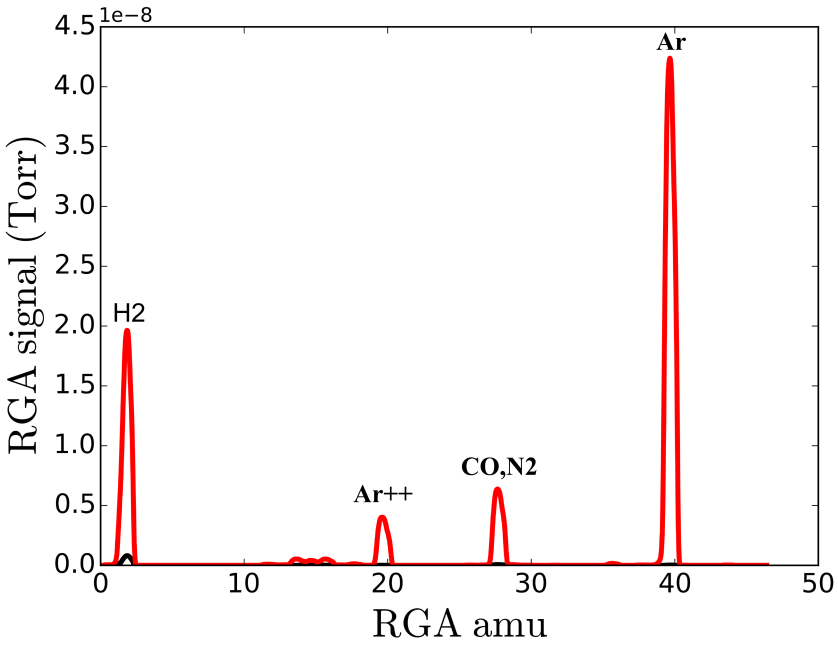

Figure 4.10: RGA trace of the contaminants in the setup when leaking in pure argon gas through a faulty leak valve. We observe many contaminants being added to the system. The main contaminants are at 2,20,28,40 amu. These peaks likely correspond to H_2, Ne, Ar^+, N_2, Ar. The black trace was taken when the leak valve was closed. Therefore all the peaks here correspond to gas coming in through the leak valve.

Here we see many contaminants effecting our setup specifically contamination from hydrogen, neon and nitrogen. The source of this contamination can be two-fold. First, the the argon line is made of a tygon tubing which is porous enough to allow these elements into the vacuum system. Second, the leak-valve used in the experiment had shown weakness in maintaining vacuum previously. To address this issue both the leak valve was replaced

and the tygon tubing was replaced with a copper one. These changes greatly remedied the situation as seen in the RGA trace below.

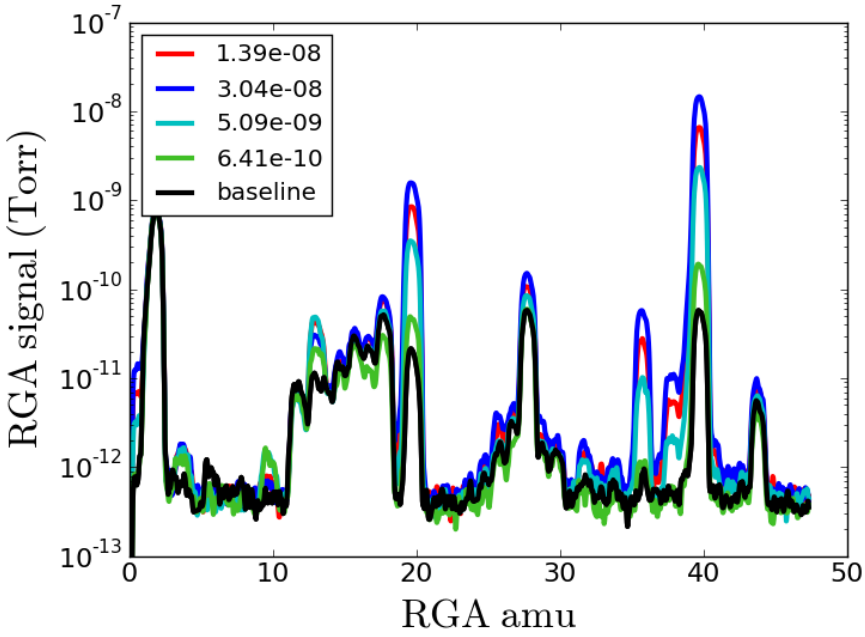

Figure 4.11: An RGA trace of the contaminants in the setup when leaking in pure argon gas at different pressures after changing the leak valve and using copper tubing. One can see the contaminants are negligibly small for Ar pressures above 10^{-8} Torr.

In Fig. 4.11 there appears to be a great reduction in the contaminants, giving more confidence that subsequent measurements will be of argon only. As a standard procedure, the RGA traces will be run for all future Ar/gas studies.

Chapter 5

Conclusion

5.1 Future Work

This experimental method can be used to explore other aspects of pressure measurements. Pressure measurements of other gases including N_2 and the other noble gases is high on the list of priorities and could provide an independent verification of their gas calibration factors. In addition, more reactive gases (such as O_2) can also be studied. Comparative studies of trap loss from the MT and MOT could be used to differentiate ground and excited state collisions and thus shed light on the excited state collision cross sections. Also, sensor atoms other than Rb could be used. Finally, by using a more dense sensor ensemble (e.g. a BEC) the sensor sensitivity could potentially be enhanced through an avalanche atom loss process. In addition, collisions with a macroscopic quantum mechanical object might offer additional opportunities to enhance the sensor sensitivity through a many-body quantum decoherence process.

5.2 Summary

Ultracold atoms provide a new way of measuring pressure in the ultra-high vacuum range. This thesis explores this idea and the possibility of using ultracold atoms as a new type of pressure standard. The operation of the two types of traps used (the MOT and MT) is examined and instructions are provided for making background collision induced loss rate measurements in each. We compare the pressure measured by cold atoms to the value reported by a NIST calibrated ionization gauge and find the gas calibration factor for Ar in agreement with the accepted value. Because this method offers a calibration free way of determining the pressure of a gas based on a fundamental atom-atom or atom-molecule collision process (assumed to be an immutable laws of physics), we believe that it is a good candidate for a primary standard in the UHV.

Bibliography

[1] A.Ashkin. Acceleration and trapping of particles by radiation pressure. *Physical Review Letters*, 24(3):156–159, 1970.

[2] M.H. Anderson, J.R. Ensher, M.R. Mattews, C.E. Wieman, and E.A. Cornell. Observation of bose-einstein condensation in a dilute atomic vapor. *Reviews of Modern Physics*, 269:198–201, 1995.

[3] Immanuel Bloch, Jean Dalibard, and Sylvain Nascimbne. Quantum simulations with ultracold quantum gases. *Nature Physics*, 8:39–44, 2002.

[4] Ying-Chen Chen, Yean-An Liao, Long Hsu, and Ite A. Yu. Simple technique for directly and accurately measuring the number of atoms in a magneto-optical trap. *Physical Review A*, 64:031401–1–031401–4, 2001.

[5] A. Clairon, P. Laurent, G. Santarelli, S. Ghezali, S. N. Lea, and M. Bahoura. A cesium fountain frequency standard: Preliminary results. *IEEE Transactions on Instrumentation and Measurement*, 44:128–131, 1995.

[6] E.A. Cornell and C.E. Wieman. Noble lecture: Bose-einstein condensation in a dilute gas, the first 70 years and some recent experiments. *Reviews of Modern Physics*, 74:875–893, 2002.

[7] K.B. Davis, M.O. Mewes, M.R. Andrews, N.J. van Drunten, D.S. Durfee, D.M. Kurn, and W. Ketterle. Bose-einstein condensation in a gas of sodium atoms. *Physical Reveiw Letters*, 75:3969–3973, 1995.

[8] J. Van Dongen, C. Zhu, D. Clement, G. Dufour, J.L. Booth, and K. W. Madison. Trap-depth determination from residual gas collisions. *Physical Review A*, 84:022708–1–022708–11, 2011.

[9] Janelle Van Dongen. *Study of background gas collisions in atomic traps.* PhD thesis, University of British Columbia, 2014.

[10] D. Fagnan. *Study of collision cross section of ultra-cold rubidium using a magneto-optic and pure magnetic trap.* PhD thesis, University of British Columbia, 2009.

[11] Markus Greiner, Olaf Mandel, Tilman Esslinger, Theodor W. Hnsch, and Immanuel Bloch. Quantum phase transition from a superfluid to a mott insulator in a gas of ultracold atoms. *Nature*, 415:39–44, 2002.

[12] T.W. Hnsch and A.L. Schawlow. Cooling of gases by laser radiation. *Optics Communications*, 13(1):68–69, 1975.

[13] J.L.Picqu and J.L. Vialle. Atomic-beam deflection and broadening by recoils due to photon absorption or emission. *Optics Communications*, 5(5):402–406, 1972.

[14] B.R. Johnson. The multichannel log-derivative method for scattering calculations. *Journal of computational physics*, 13:445–449, 1973.

[15] Wolfgang Ketterle. Noble lecture: When atoms behave as waves: Bose-einstein condensation and the atom laser. *Reviews of Modern Physics*, 74:1131–1151, 2002.

[16] John Kitching, Svenja Knappe, and Elizabeth A. Donley. Atomic sensors - a review. *IEEE Sensors Journal*, 11:1749–1758, 2011.

[17] L. D. Landau and E. M. Lifshitz. *Quantum Mechanics: Non-relativistic theory*, volume 3 of *Course of Theoretical Physics*. Pergamon Press, Oxford; New York, third edition, 1989, c1977.

[18] Paul D. Lett, Richard N. Watts, Christoph I. Westbrook, William D. Phillips, Phillip L. Gould, and Harold J. Metcalf. Observation of atoms laser cooled below the doppler limit. *Physical Reveiw Letters*, 61(2):169–172, 1988.

[19] Y.J. Lin, A.R. Perry, R.L. Compton, I.B. Spielman, and J.V. Porto. Rapid production of 87rb bose-einstein condensates in a combined magnetic and optical potential. *Physical Review A*, 79:063631–1–063631–8, 2009.

[20] Harold J. Metcalf and Peter van der Straten. *Laser Cooling and Trapping*. Springer, New York, 1999.

[21] Wolfgang Petrich, Micheal H. Anderson, Jason R. Ensher, and Eric A. Cornell. Stable, tightly confining magnetic trap for evaporative cooling of neutral atoms. *Physical Reveiw Letters*, 74(17):3352–3355, 1995.

[22] E.L. Raab, M. Prentiss, Alex Cable, Steven Chu, and D.E. Pritchard. Trapping of neutral sodium atoms with radiation pressure. *Physical Reveiw Letters*, 59(23):2631–2634, 1987.

[23] Philipp-Immanuel Schneider and Alejandro Sanez. Quantum computation with ultracold atoms in a driven optical lattice. *Physical Review A*, 85:050304–1–050304–5, 2012.

[24] Robert L. Summers. *Empirical Observations on the Sensitivity of Hot Cathode Ionization Type Vacuum Gages*. NASA, 1969.